



A phase-field description of dynamic brittle fracture

Michael J. Borden^{a,*}, Clemens V. Verhoosel^b, Michael A. Scott^a, Thomas J.R. Hughes^a, Chad M. Landis^c

^aInstitute for Computational Engineering and Sciences, The University of Texas at Austin, 1 University Station C0200, Austin, TX 78712, USA

^bEindhoven University of Technology, Mechanical Engineering, Numerical Methods in Engineering, PO Box 513, WH 2.115, 5600 MB Eindhoven, The Netherlands

^cAerospace Engineering and Engineering Mechanics, The University of Texas at Austin, 1 University Station C0600, Austin, TX 78712, USA

ARTICLE INFO

Article history:

Received 10 May 2011

Received in revised form 31 October 2011

Accepted 11 January 2012

Available online 26 January 2012

Keywords:

Phase field

Fracture mechanics

Isogeometric analysis

Adaptive refinement

T-splines

ABSTRACT

In contrast to discrete descriptions of fracture, phase-field descriptions do not require numerical tracking of discontinuities in the displacement field. This greatly reduces implementation complexity. In this work, we extend a phase-field model for quasi-static brittle fracture to the dynamic case. We introduce a phase-field approximation to the Lagrangian for discrete fracture problems and derive the coupled system of equations that govern the motion of the body and evolution of the phase-field. We study the behavior of the model in one dimension and show how it influences material properties. For the temporal discretization of the equations of motion, we present both a monolithic and staggered time integration scheme. We study the behavior of the dynamic model by performing a number of two and three dimensional numerical experiments. We also introduce a local adaptive refinement strategy and study its performance in the context of locally refined T-splines. We show that the combination of the phase-field model and local adaptive refinement provides an effective method for simulating fracture in three dimensions.

© 2012 Elsevier B.V. All rights reserved.

1. Introduction

The prevention of fracture-induced failure is a major constraint in engineering designs, and the numerical simulation of fracture processes often plays a key role in design decisions. As a consequence, a wide variety of fracture models have been proposed. A particularly successful model is provided by Griffith's theory for brittle fracture, which relates crack nucleation and propagation to a critical value of the energy release rate. A general concept in the Griffith's-type brittle fracture models is that upon the violation of the critical energy release rate a fully opened crack is nucleated or propagated. As a consequence, the process zone, i.e., the zone in which the material transitions from the undamaged to the damaged state is lumped into a single point at the crack tip.

Due to the complexity of fracture processes in engineering applications, numerical methods play a crucial role in fracture analyses. In particular, finite element methods are used extensively in conjunction with Griffith's-type linear elastic fracture mechanics models. Among the most commonly used finite element models are the virtual crack closure technique (see [32]), and, in more recent years, the extended finite element method introduced by Moës et al. [40]. All of these approaches represent cracks as discrete discontinuities, either by inserting discontinuity lines by means of remeshing strategies, or by enriching the displacement

field with discontinuities using the partition of unity method of Babuška and Melenk [4]. Tracing the evolution of complex fracture surfaces has, however, proven to be a tedious task, particularly in three dimensions.

Recently, alternative methods for the numerical simulation of brittle fracture have emerged. In these approaches, discontinuities are not introduced into the solid. Instead, the fracture surface is approximated by a phase-field, which smoothes the boundary of the crack over a small region. The major advantage of using a phase-field is that the evolution of fracture surfaces follows from the solution of a coupled system of partial differential equations. Implementation does not require the fracture surfaces to be tracked algorithmically. This is in contrast to the complexity of many discrete fracture models, and is anticipated to be particularly advantageous when multiple branching and merging cracks are considered in three dimensions.

A phase-field model for quasi-static brittle fracture emanated from the work of Francfort and co-workers on the variational formulation for Griffith's-type fracture models. The genesis of the approach is due to Francfort and Marigo [21], and that of the phase-field implementation to Bourdin et al. [13] (see [14] for a comprehensive overview). The variational formulation for quasi-static brittle fracture leads to an energy functional that closely resembles the potential presented by Mumford and Shah [41], which is encountered in image segmentation. A phase-field approximation of the Mumford-Shah potential, based on the theory of Γ -convergence, was presented by Ambrosio and Tortorelli [1]. As

* Corresponding author. Tel.: +1 512 475 6399; fax: +1 512 323 7508.

E-mail address: mborden@ices.utexas.edu (M.J. Borden).

discussed by Bourdin et al. [14], this approximation was adopted to facilitate the numerical solution of their variational formulation. Recently, this model has been applied in a dynamic setting by Bourdin et al. [15], Larsen et al. [35], and Larsen [34], but application to structures of engineering interest has not been considered.

An alternative quasi-static formulation of this phase-field approximation has been presented in the recent work of Miehe et al. [37] and Miehe et al. [38]. In this formulation, the phase-field approximation follows from continuum mechanics and thermodynamic arguments. Besides the provision of an alternative derivation, Miehe et al. [37] also added various features to the model that are key to its application to engineering structures.

Independently from the phase-field formulation based on Griffith's theory, dynamic phase-field fracture models have been developed based on Landau–Ginzburg type phase-field evolution equations, e.g., Karma et al. [31]. However, we favor the phase-field formulation of the Bourdin-type since the physical properties of Griffith's theory are well understood and have proven useful in engineering applications.

In this contribution we extend the quasi-static model presented by Miehe et al. [37] to the dynamic case. We begin by formulating the Lagrangian for the discrete fracture problem in terms of the displacements and the phase-field approximation of the crack path. Then, using the Euler–Lagrange equations of this approximation, we derive the strong form equations of motion. A detailed analysis of the analytical one-dimensional solution to the strong form equations is then presented. In this analysis we show that although the length-scale parameter associated with the phase-field approximation is introduced as a numerical parameter it is, in fact, a material parameter that influences the critical stress at which crack nucleation occurs.

The numerical solution of the strong form of the equations of motion requires a spatial and temporal discretization. We formulate the spatial discretization by means of the Galerkin method. In this work, we have used NURBS and T-spline basis functions as the finite dimensional approximations to the function spaces of the weak form. However, we note that standard C^0 -continuous finite elements could also be used. For the temporal discretization, we present monolithic and staggered time integration schemes. The monolithic scheme requires solution of the coupled equations simultaneously. For the staggered scheme, the displacements (via the momentum equation) and phase-field (via the phase-field equation) are solved for separately. This provides flexibility in solution strategies by allowing the momentum equations to be solved either implicitly or explicitly.

To conclude this paper, we study the behavior of the model by performing a number of numerical benchmark experiments for crack propagation and branching. These experiments show that the phase-field model can capture complex crack behavior in both two and three dimensions, without introducing any ad hoc criteria for crack nucleation and branching. In addition, we propose an adaptive refinement strategy that allows for the efficient simulation of complex crack patterns. We show that adaptive refinement maintains accuracy while providing greater efficiency in terms of the number of degrees-of-freedom. Finally, we apply the adaptive refinement strategy to a three-dimensional problem. This final problem illustrates the potential strength of the phase-field model, which is the ability to efficiently model dynamic fracture in three-dimensions.

2. Formulation

We briefly introduce Griffith's theory for dynamic brittle fracture in bodies with arbitrarily discrete cracks. We then present a phase-field formulation as a continuous approximation of the dis-

crete fracture model. We conclude this section with a study of analytical solutions of the phase-field in the one-dimensional quasi-static case, which reveals many interesting features of the model.

2.1. Griffith's theory of brittle fracture

We consider an arbitrary body $\Omega \subset \mathbb{R}^d$ (with $d \in \{1, 2, 3\}$) with external boundary $\partial\Omega$ and internal discontinuity boundary Γ (see Fig. 1a). The displacement of a point $\mathbf{x} \in \Omega$ at time $t \in [0, T]$ is denoted by $\mathbf{u}(\mathbf{x}, t) \in \mathbb{R}^d$. Spatial components of vectors and tensors are indexed by $i, j = 1, \dots, d$. The displacement field satisfies time-dependent Dirichlet boundary conditions, $u_i(\mathbf{x}, t) = g_i(\mathbf{x}, t)$, on $\partial\Omega_{g_i} \subseteq \partial\Omega$, and time-dependent Neumann boundary conditions on $\partial\Omega_{h_i} \subseteq \partial\Omega$. We assume small deformations and deformation gradients, and define the infinitesimal strain tensor, $\boldsymbol{\varepsilon}(\mathbf{x}, t) \in \mathbb{R}^{d \times d}$, with components

$$\varepsilon_{ij} = u_{(ij)} = \frac{1}{2} \left(\frac{\partial u_i}{\partial x_j} + \frac{\partial u_j}{\partial x_i} \right) \quad (1)$$

as an appropriate deformation measure. We assume isotropic linear elasticity, such that the elastic energy density is given by

$$\psi_e(\boldsymbol{\varepsilon}) = \frac{1}{2} \lambda \varepsilon_{ii} \varepsilon_{jj} + \mu \varepsilon_{ij} \varepsilon_{ij} \quad (2)$$

with λ and μ the Lamé constants. Note that we use the Einstein summation convention on repeated indices.

The evolving internal discontinuity boundary, $\Gamma(t)$, represents a set of discrete cracks. In accordance with Griffith's theory of brittle fracture, the energy required to create a unit area of fracture surface is equal to the critical fracture energy density \mathcal{G}_c .¹ The total potential energy of the body, Ψ_{pot} , being the sum of the elastic energy and the fracture energy, is then given by

$$\Psi_{pot}(\mathbf{u}, \Gamma) = \int_{\Omega} \psi_e(\nabla^s \mathbf{u}) d\mathbf{x} + \int_{\Gamma} \mathcal{G}_c d\mathbf{x}, \quad (3)$$

where we have defined the symmetric gradient operator, $\nabla^s : \mathbf{u} \rightarrow \boldsymbol{\varepsilon}$, as a mapping from the displacement field to the strain field. Since brittle fracture is assumed, the fracture energy contribution is merely the critical fracture energy density integrated over the fracture surface. In the case of small deformations, irreversibility of the fracture process dictates that $\Gamma(t) \subseteq \Gamma(t + \Delta t)$ for all $\Delta t > 0$. Hence, translation of cracks through the domain is prohibited, but cracks can extend, branch, and merge.

The kinetic energy of the body Ω is given by

$$\Psi_{kin}(\dot{\mathbf{u}}) = \frac{1}{2} \int_{\Omega} \rho \dot{u}_i \dot{u}_i d\mathbf{x} \quad (4)$$

with $\dot{\mathbf{u}} = \frac{\partial \mathbf{u}}{\partial t}$ and ρ the mass density of the material. Combined with the potential energy (3) this renders the Lagrangian for the discrete fracture problem as

$$\begin{aligned} L(\mathbf{u}, \dot{\mathbf{u}}, \Gamma) &= \Psi_{kin}(\dot{\mathbf{u}}) - \Psi_{pot}(\mathbf{u}, \Gamma) \\ &= \int_{\Omega} \left[\frac{1}{2} \rho \dot{u}_i \dot{u}_i - \psi_e(\nabla^s \mathbf{u}) \right] d\mathbf{x} - \int_{\Gamma} \mathcal{G}_c d\mathbf{x}. \end{aligned} \quad (5)$$

The Euler–Lagrange equations of this functional determine the motion of the body. From a numerical standpoint, tracking the evolving discontinuity boundary, Γ , often requires complex and costly computations. This is particularly so when interactions between multiple cracks (even in two dimensions), or complex shaped cracks in three dimensions are considered. Of particular interest in the case of dynamic fracture simulations, as considered in this work, is the ability to robustly model crack branching. In the remainder of this

¹ This critical fracture energy density is commonly referred to as the critical energy release rate, or, in the context of cohesive zone models, the fracture toughness.

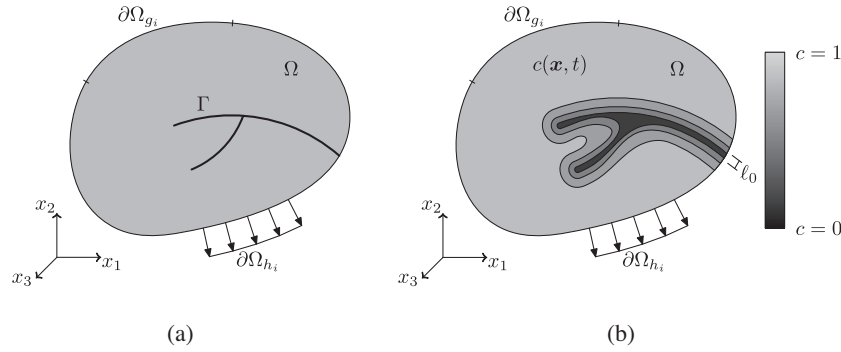


Fig. 1. (a) Schematic representation of a solid body Ω with internal discontinuity boundaries Γ . (b) Approximation of the internal discontinuity boundaries by the phase-field $c(\mathbf{x}, t)$. The model parameter ℓ_0 controls the width of the failure zone.

work we pursue a formulation which is capable of handling cracks of arbitrary topological complexity.

2.2. Phase-field approximation

In order to circumvent the problems associated with numerically tracking the propagating discontinuity representing a crack, we approximate the fracture surface, Γ , by a phase-field, $c(\mathbf{x}, t) \in [0, 1]$. The value of this phase-field is equal to 1 away from the crack and is equal to 0 inside the crack (see Fig. 1b). We employ the approximation as discussed in Miehe et al. [37], which is essentially an extension of the phase-field approximation introduced by Bourdin et al. [14].² As in Bourdin et al. [14], we approximate the fracture energy by

$$\int_{\Gamma} \mathcal{G}_c d\mathbf{x} \approx \int_{\Omega} \mathcal{G}_c \left[\frac{(c-1)^2}{4\ell_0} + \ell_0 \frac{\partial c}{\partial x_i} \frac{\partial c}{\partial x_i} \right] d\mathbf{x}, \quad (6)$$

where $\ell_0 \in \mathbb{R}^+$ is a model parameter that controls the width of the smooth approximation of the crack. From Eq. (6) it is clear that a crack is represented by regions where the phase-field, $c(\mathbf{x}, t)$, goes to zero. As elaborated by e.g. Bourdin et al. [14], in the limit of the length scale ℓ_0 going to zero, the phase-field approximation converges to the discrete fracture surface.

To model the loss of material stiffness in the failure zone (i.e., the phase-field approximation of the fracture surface), we follow Miehe et al. [37] and define the elastic energy as

$$\psi_e(\boldsymbol{\varepsilon}, c) = [(1-k)c^2 + k]\psi_e^+(\boldsymbol{\varepsilon}) + \psi_e^-(\boldsymbol{\varepsilon}), \quad (7)$$

where ψ_e^+ and ψ_e^- are the strain energies computed from the positive and negative components of the strain tensor, respectively, defined through a spectral decomposition of strain. Let

$$\boldsymbol{\varepsilon} = \mathbf{P}\boldsymbol{\Lambda}\mathbf{P}^T \quad (8)$$

where \mathbf{P} consists of the orthonormal eigenvectors of $\boldsymbol{\varepsilon}$ and $\boldsymbol{\Lambda} = \text{diag}(\lambda_1, \lambda_2, \lambda_3)$ is a diagonal matrix of principal strains. We define

$$\boldsymbol{\varepsilon}^+ = \mathbf{P}\boldsymbol{\Lambda}^+\mathbf{P}^T, \quad (9)$$

$$\boldsymbol{\varepsilon}^- = \mathbf{P}\boldsymbol{\Lambda}^-\mathbf{P}^T, \quad (10)$$

where

$$\boldsymbol{\Lambda}^+ = \text{diag}(\langle \lambda_1 \rangle, \langle \lambda_2 \rangle, \langle \lambda_3 \rangle), \quad (11)$$

$$\boldsymbol{\Lambda}^- = \boldsymbol{\Lambda} - \boldsymbol{\Lambda}^+ \quad (12)$$

² For the most part, we adopt the notation introduced by Bourdin et al. [14], the exception being the use of k in place of η for the model parameter that controls conditioning of the linear system. In Miehe et al. [37], use is made of a damage field $d(\mathbf{x}, t) = 1 - c(\mathbf{x}, t)$, and a length scale $l = 2\ell_0$ to control the width of the failure zone.

and

$$\langle x \rangle = \begin{cases} x & x > 0, \\ 0 & x \leq 0. \end{cases} \quad (13)$$

Then

$$\psi_e^+(\boldsymbol{\varepsilon}) = \frac{1}{2} \lambda \langle \text{tr} \boldsymbol{\varepsilon} \rangle^2 + \mu \text{tr}[(\boldsymbol{\varepsilon}^+)^2] \quad (14)$$

and

$$\psi_e^-(\boldsymbol{\varepsilon}) = \frac{1}{2} \lambda (\text{tr} \boldsymbol{\varepsilon} - \langle \text{tr} \boldsymbol{\varepsilon} \rangle)^2 + \mu \text{tr}[(\boldsymbol{\varepsilon} - \boldsymbol{\varepsilon}^+)^2]. \quad (15)$$

This decomposition is somewhat different from the one used in Amor et al. [3]. In our formulation, Amor et al. [3] would be

$$\psi_e(\boldsymbol{\varepsilon}, c) = \frac{\kappa}{2} (\text{tr} \boldsymbol{\varepsilon} - \langle \text{tr} \boldsymbol{\varepsilon} \rangle)^2 + [(1-k)c^2 + k] \left(\frac{\kappa}{2} \langle \text{tr} \boldsymbol{\varepsilon} \rangle^2 + \mu \text{tr}[(\boldsymbol{\varepsilon}^{\text{dev}})^2] \right), \quad (16)$$

where κ is the bulk modulus and $\boldsymbol{\varepsilon}^{\text{dev}}$ is the deviatoric strain tensor. In the Amor et al. [3] model, expansive volumetric strain energy, as measured by $\langle \text{tr} \boldsymbol{\varepsilon} \rangle$, and deviatoric strain energy, are subjected to damage, but not compressive volumetric strain energy. We note a difference of this model compared with the model we use is that, as is evident from (16), all three principal strains could be negative, but the deviatoric strain energy would experience damage, unlike the model we use. However, the intent of both models is similar, that is, to maintain resistance in compression and, in particular, during crack closure. Del Piero et al. [19] provide a large deformation definition of strain energy, but they do not decompose the strain energy into positive and negative parts to maintain resistance to compression. Rather, they rely on residual elasticity provided by the parameter k and the fact that as the Jacobian determinate goes to zero, the strain energy approaches positive infinity.

By only applying the phase-field parameter to the tensile part of the elastic energy density, we prohibit crack propagation under compression. This model feature has been observed to be particularly important in dynamic simulations, as stress waves reflecting from domain boundaries tend to create physically unrealistic fracture patterns. The model parameter $k \ll 1$ was introduced in Ambrosio and Tortorelli [2] as a way to avoid ill-posedness. Although it has been used in numerous numerical implementations and theoretical papers (see [3,5,11–13,16,17,19,22,33]) proved later it was not necessary in order to obtain Γ -convergence. We have tested the necessity of setting $k > 0$ in our formulation numerically and we have also found its inclusion to be unnecessary. In fact, all calculations presented in this paper set $k = 0$.

Substitution of the phase-field approximations for the fracture energy (6) and the elastic energy density (7) into the Lagrange energy functional (5) yields

$$L_e(\mathbf{u}, \dot{\mathbf{u}}, c) = \int_{\Omega} \left(\frac{1}{2} \rho \dot{\mathbf{u}}_i \dot{\mathbf{u}}_i - [(1-k)c^2 + k] \psi_e^+ (\nabla^s \mathbf{u}) - \psi_e^- (\nabla^s \mathbf{u}) \right) d\mathbf{x} \\ - \int_{\Omega} \mathcal{G}_c \left[\frac{(c-1)^2}{4\ell_0} + \ell_0 \frac{\partial c}{\partial x_i} \frac{\partial c}{\partial x_i} \right] d\mathbf{x}. \quad (17)$$

Note that in order to conserve mass the kinetic energy term is unaffected by the phase-field approximation. The dependence of the Lagrange energy functional on the propagating discontinuity boundary is now captured by the phase-field, $c(\mathbf{x}, t)$, which simplifies the numerical treatment of the model. In Miehe et al. [37] an additional viscosity contribution is introduced. For the dynamic simulations performed within this study no beneficial effects of this viscosity parameter were encountered, and hence this term is omitted for brevity.

Now that we have formulated the Lagrangian in terms of the independent fields $\mathbf{u}(\mathbf{x}, t)$ and $c(\mathbf{x}, t)$, we can use the Euler–Lagrange equations to arrive at the strong form equations of motion

$$\begin{cases} \frac{\partial \sigma_{ij}}{\partial x_j} = \rho \ddot{u}_i & \text{on } \Omega \times]0, T[, \\ \left(\frac{4\ell_0(1-k)\psi_e^+}{\mathcal{G}_c} + 1 \right) c - 4\ell_0^2 \frac{\partial^2 c}{\partial x_i^2} = 1 & \text{on } \Omega \times]0, T[, \end{cases} \quad (18)$$

where $\ddot{\mathbf{u}} = \frac{\partial^2 \mathbf{u}}{\partial t^2}$ and the Cauchy stress tensor $\boldsymbol{\sigma} \in \mathbb{R}^{d \times d}$ is defined by

$$\sigma_{ij} = [(1-k)c^2 + k] \frac{\partial \psi_e^+}{\partial \varepsilon_{ij}} + \frac{\partial \psi_e^-}{\partial \varepsilon_{ij}}. \quad (19)$$

These equations of motion can be solved to find both the displacement field $\mathbf{u}(\mathbf{x}, t)$ and phase-field $c(\mathbf{x}, t)$. The irreversibility condition $\Gamma(t) \subseteq \Gamma(t + \Delta t)$ is enforced in the strong-form equations by introducing a strain-history field, \mathcal{H} , which satisfies the Kuhn–Tucker conditions for loading and unloading

$$\psi_e^+ - \mathcal{H} \leq 0, \quad \dot{\mathcal{H}} \geq 0, \quad \dot{\mathcal{H}}(\psi_e^+ - \mathcal{H}) = 0 \quad (20)$$

(see [37] for motivation on the introduction of \mathcal{H}). After substituting \mathcal{H} for ψ_e^+ in (18)₂ we get the modified strong form equations of motion

$$(S) \begin{cases} \frac{\partial \sigma_{ij}}{\partial x_j} = \rho \ddot{u}_i & \text{on } \Omega \times]0, T[, \\ \left(\frac{4\ell_0(1-k)\mathcal{H}}{\mathcal{G}_c} + 1 \right) c - 4\ell_0^2 \frac{\partial^2 c}{\partial x_i^2} = 1 & \text{on } \Omega \times]0, T[. \end{cases} \quad (21)$$

The equations of motion are subject to the boundary conditions

$$(S : BC) \begin{cases} u_i = g_i & \text{on } \partial\Omega_{g_i} \times]0, T[, \\ \sigma_{ij} n_j = h_i & \text{on } \partial\Omega_{h_i} \times]0, T[, \\ \frac{\partial c}{\partial x_i} n_i = 0 & \text{on } \partial\Omega \times]0, T[\end{cases} \quad (22)$$

with $g_i(\mathbf{x}, t)$ and $h_i(\mathbf{x}, t)$ being prescribed on $\partial\Omega_{g_i}$ and $\partial\Omega_{h_i}$, respectively, for all $t \in]0, T[$, and with $\mathbf{n}(\mathbf{x})$ being the outward-pointing normal vector of the boundary.

In addition, the equations of motion (21) are supplemented with initial conditions

$$(S : IC) \begin{cases} \mathbf{u}(\mathbf{x}, 0) = \mathbf{u}_0(\mathbf{x}) & \mathbf{x} \in \Omega, \\ \dot{\mathbf{u}}(\mathbf{x}, 0) = \mathbf{v}_0(\mathbf{x}) & \mathbf{x} \in \Omega, \\ \mathcal{H}(\mathbf{x}, 0) = \mathcal{H}_0(\mathbf{x}) & \mathbf{x} \in \Omega \end{cases} \quad (23)$$

for both the displacement field and the strain-history field. $\mathcal{H}_0(\mathbf{x})$, can be used to model pre-existing cracks or geometrical features (see Appendix A for details).

2.3. Analytical solutions of the one-dimensional quasi-static problem

To illustrate various properties of the phase-field formulation for brittle fracture, we study the analytical solution to the boundary value problem introduced in the previous section. We restrict

ourselves to the one-dimensional domain $\Omega = \mathbb{R}$ ($d = 1$) and ignore all temporal derivatives. In addition we assume the parameter k to be equal to zero, and the strain field to be non-negative (i.e., $\psi_e^- = 0$ such that $\psi_e = \frac{1}{2} c^2 E \varepsilon^2$). Under these assumptions, the strong form equilibrium equations (21) reduce to

$$\begin{cases} \frac{d\sigma}{dx} = 0 & \text{on } \mathbb{R} \times]0, T[, \\ \left(\frac{4\ell_0 \mathcal{H}}{\mathcal{G}_c} + 1 \right) c - 4\ell_0^2 \frac{d^2 c}{dx^2} = 1 & \text{on } \mathbb{R} \times]0, T[\end{cases} \quad (24)$$

with $\sigma = c^2 E \varepsilon$. By virtue of (24)₁, the stress σ is constant over the domain. One-dimensional analyses of related phase-field models have appeared previously in [3,7,42].

2.3.1. Homogeneous solution

We first study the homogeneous solution by ignoring all spatial derivatives of c . This approach has been previously utilized by others (see e.g. [3,12,20,42]) to investigate the stress–strain response of damage-elastic models. From the phase-field equation we then obtain

$$c_{\text{hom}} = \begin{cases} \left(\frac{2\ell_0 E}{\mathcal{G}_c} \varepsilon_{\text{hom}}^2 + 1 \right)^{-1} & \psi_e^+ = \mathcal{H}, \\ \left(\frac{4\ell_0 \mathcal{H}}{\mathcal{G}_c} + 1 \right)^{-1} & \psi_e^+ < \mathcal{H}, \end{cases} \quad (25)$$

where c_{hom} and ε_{hom} are the homogeneous phase-field and strain, respectively. Substitution of this result into the constitutive equation yields the homogeneous stress as a function of the homogeneous strain

$$\sigma_{\text{hom}} = \begin{cases} \left(\frac{2\ell_0 E}{\mathcal{G}_c} \varepsilon_{\text{hom}}^2 + 1 \right)^{-2} E \varepsilon_{\text{hom}} & \psi_e^+ = \mathcal{H}, \\ \left(\frac{4\ell_0 \mathcal{H}}{\mathcal{G}_c} + 1 \right)^{-2} E \varepsilon_{\text{hom}} & \psi_e^+ < \mathcal{H}. \end{cases} \quad (26)$$

Fig. 2(a) shows a characteristic plot of the homogeneous stress versus the homogeneous strain. Fig. 2(b) shows the corresponding evolution of the homogeneous phase-field parameter. Note that the plotted results have been non-dimensionalized as outlined in Appendix B. It is observed that as the strain is increased, initially the stress also increases. This increase in stress is accompanied by a gradual decrease of the phase-field parameter. At some point, a critical stress level, σ_c , is reached after which both the stress and the phase-field decrease in value upon an increase in strain. In unloading the phase-field remains constant, which results in secant unloading behavior in the stress–strain curve.

The critical value for the stress, and corresponding value for the strain, are found as

$$\sigma_c = \frac{9}{16} \sqrt{\frac{E \mathcal{G}_c}{6\ell_0}}, \quad \varepsilon_c = \sqrt{\frac{\mathcal{G}_c}{6\ell_0 E}}. \quad (27)$$

From these expressions it is observed that the critical stress will increase as ℓ_0 decreases. In the limit as ℓ_0 goes to zero, i.e., when the phase-field formulation coincides with the discrete fracture formulation, the crack nucleation stress becomes infinite. This observation is consistent with the properties of Griffith's theory, which only allows for crack nucleation at stress singularities. It is interesting to note that the critical value for the phase-field is independent of the model and material parameters

$$c_c = \sqrt{\frac{\sigma_c}{E \varepsilon_c}} = \frac{3}{4}. \quad (28)$$

This implies that, no matter what parameters are used, a 25% reduction in the phase-field is established prior to crack nucleation at places where a crack emerges.

By virtue of the preceding analysis, we might view ℓ_0 as a material parameter since it influences the critical stress. The issue as to

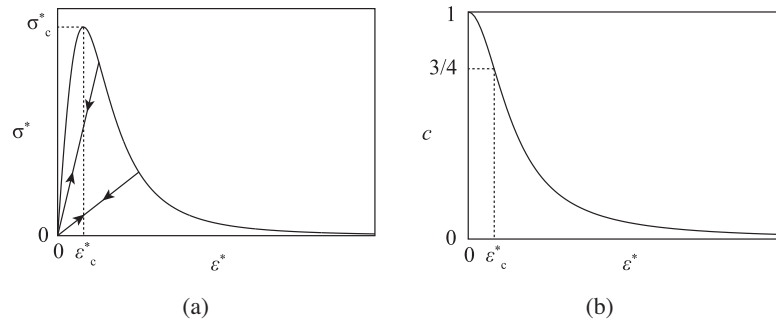


Fig. 2. One-dimensional characteristic stress–strain (a) and phase-field–strain (b) curves for the homogeneous solution. Note that the value of ℓ_0 influences the maximum tensile stress, see (27).

whether or not ℓ_0 is a numerical regularization parameter or a material parameter has been discussed in Amor et al. [3]. See also the import results presented in Pham et al. [42].

2.3.2. Non-homogenous solution

Additional interesting features of the model can be observed from the non-homogeneous solution of the one-dimensional static problem (24). If we ignore the irreversibility in the model, i.e. we take $\mathcal{H} = \frac{1}{2}E\epsilon^2$, we can combine the constitutive and phase-field equations to yield the non-linear ordinary differential equation

$$\left(\frac{2\ell_0\sigma^2}{c^4E\mathcal{G}_c} + 1\right)c - 4\ell_0^2\frac{d^2c}{dx^2} = 1. \quad (29)$$

A solution for the phase-field, $c(x)$, with a crack at $x = 0$ is found by supplementing this differential equation with the boundary condition $\lim_{x \rightarrow \pm\infty} c(x) = c_{\text{hom}}(\sigma)$, which implies that the phase-field gradient vanishes far away from the crack. It is important to note that the homogeneous solution to the phase-field is dependent on the stress, σ , as elaborated in the previous section. In addition to the far-field boundary condition, we require the solution to be symmetric and differentiable at every point except for $x = 0$.

The first step in finding the non-homogeneous solution to the phase-field problem is to multiply Eq. (29) with $\frac{dc}{dx}$ and make use of the fact that, by (24), σ is constant, to obtain

$$\frac{d}{dx} \left[-\frac{\ell_0\sigma^2}{c^2E\mathcal{G}_c} + \frac{c^2}{2} - 2\ell_0^2 \left(\frac{dc}{dx} \right)^2 - c \right] = 0. \quad (30)$$

Since we require the solution to be symmetric around $x = 0$, we integrate this expression from x to infinity for positive values of x , and from minus infinity to x when x is negative. Since we have specified the crack to be centered at $x = 0$, we require the phase-field to have a minimum at $x = 0$. From these requirements, we obtain

$$\frac{dc}{dx} = \text{sgn}(x) \sqrt{\frac{1}{2\ell_0^2} \left(-\frac{\ell_0\sigma^2}{c^2E\mathcal{G}_c} + \frac{c^2}{2} - c - a \right)} \quad (31)$$

where the coefficient a follows from the far-field boundary condition as

$$a = -\frac{\ell_0\sigma^2}{c_{\text{hom}}^2E\mathcal{G}_c} + \frac{c_{\text{hom}}^2}{2} - c_{\text{hom}}. \quad (32)$$

By definition, substitution of the homogeneous solution $c_{\text{hom}}(\sigma)$ into Eq. (31) yields a zero phase-field gradient. An analytical non-homogeneous solution to Eq. (29) can be found for the case of a fully developed crack, i.e. for $\sigma = 0$ (no stress carrying capability) and $c_{\text{hom}}(0) = 1$. In this case, Eq. (31) reduces to

$$\frac{dc}{dx} = \text{sgn}(x) \frac{1-c}{2\epsilon} \quad (33)$$

and, assuming $c(0) = 0$, we find

$$c = 1 - \exp\left(-\frac{|x|}{2\ell_0}\right) \quad (34)$$

as the solution that satisfies the specified boundary conditions. Note that this is the exact function used by Miehe et al. [37] to derive their phase field formulation. This function is exactly the construction of the recovery sequence for the Γ -convergence proof, originally given in Ambrosio and Tortorelli [2]. Note that its construction is also justified in much less technical terms in [14, Section 8.1.1].

The unique non-homogeneous solution can also be constructed for $\sigma > 0$. In this case, a second admissible phase-field value, smaller than the homogeneous solution, c_{hom} , for which the gradient is equal to zero can be found. This phase-field value corresponds to the value of the phase-field at the center of the crack, and is denoted by c_{crack} . Since the phase-field increases monotonically from c_{crack} at the center of the crack (at $x = 0$) to c_{hom} far away from the crack ($x = \pm\infty$), we find the coordinates $0 < \pm x < \infty$ at which the phase-field is equal to $c_{\text{crack}} < c(x) < c_{\text{hom}}$ by evaluation of

$$x = \pm \int_{c_{\text{crack}}}^{c(x)} \left[\frac{1}{2\ell_0^2} \left(-\frac{\ell_0\sigma^2}{c^2E\mathcal{G}_c} + \frac{c^2}{2} - c - a \right) \right]^{-\frac{1}{2}} d\bar{c}. \quad (35)$$

In non-dimensional form with the non-dimensional constant $C_h = 1$, (35) becomes

$$x^* = \pm \int_{c_{\text{crack}}}^{c(L_0x^*)} \left[\frac{1}{2(\ell_0^*)^2} \left(-\frac{\ell_0^*(\sigma^*)^2}{\bar{c}^2} + \frac{\bar{c}^2}{2} - \bar{c} - a^* \right) \right]^{-\frac{1}{2}} d\bar{c}. \quad (36)$$

Evaluating this integral numerically for $\sigma = \beta\sigma_c$ with various values of $\beta \in]0, 1[$ we get the solutions shown in Fig. 3 (note that the presented results have again been non-dimensionalized and merely depend on the parameter β). It is interesting to note that, except for the limiting case of a fully developed crack, the solution to the phase-field is smooth at the center of the crack.

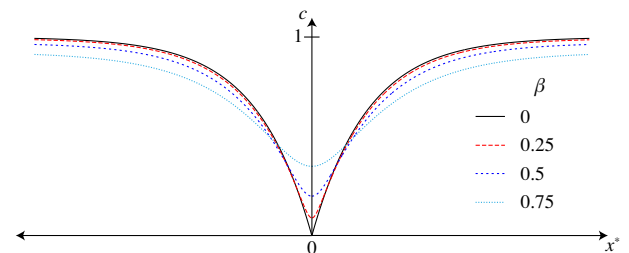


Fig. 3. One-dimensional solution of the phase field formulation for various values of the stress ratio $\beta = \frac{\sigma}{\sigma_c} = \frac{\sigma^*}{\sigma_c^*}$. Note that, except for the limiting case $\beta = 0$, the phase-field is smooth at the center of the crack ($x^* = 0$).

For further results on non-homogeneous solutions of one-dimensional problems see Pham and Marigo [43] and Pham et al. [42].

3. Numerical formulation

The numerical solution of (21) requires a spatial and temporal discretization. In this section we formulate the spatial discretization by means of the Galerkin method and we introduce two temporal discretization schemes: a monolithic implicit scheme and a staggered scheme in which the momentum equation and phase-field equation are solve separately, and in which the momentum equation may be solved either by an explicit or implicit scheme.

3.1. Continuous problem in the weak form

For the weak form of the problem we define the trial solution spaces \mathcal{S}_t for the displacements and $\tilde{\mathcal{S}}_t$ for the phase-field as

$$\mathcal{S}_t = \{\mathbf{u}(t) \in (H^1(\Omega))^d | u_i(t) = g_i \text{ on } \partial\Omega_{g_i}\}, \quad (37)$$

$$\tilde{\mathcal{S}}_t = \{c(t) \in H^1(\Omega)\}. \quad (38)$$

Similarly, the weighting function spaces are defined as

$$\mathcal{V} = \{\mathbf{w} \in (H^1(\Omega))^d | w_i = 0 \text{ on } \partial\Omega_{g_i}\} \quad (39)$$

$$\tilde{\mathcal{V}} = \{q \in H^1(\Omega)\}. \quad (40)$$

Multiplying the equations in (21) by the appropriate weighting functions and applying integration by parts leads to the weak formulation:

$$(W) \begin{cases} \text{Given } \mathbf{g}, \mathbf{h}, \mathbf{u}_0, \dot{\mathbf{u}}_0, \text{ and } c_0 \text{ find } \mathbf{u}(t) \in \mathcal{S}_t \text{ and } c(t) \in \tilde{\mathcal{S}}_t, t \in [0, T], \text{ such that for all } \\ \mathbf{w} \in \mathcal{V} \text{ and for all } q \in \tilde{\mathcal{V}}, \\ (\rho \ddot{\mathbf{u}}, \mathbf{w})_\Omega + (\boldsymbol{\sigma}, \nabla \mathbf{w})_\Omega = (\mathbf{h}, \mathbf{w})_{\partial\Omega_h}, \\ \left(\left(\frac{4\ell_0(1-k)\mathcal{H}}{\mathcal{G}_c} + 1 \right) c, q \right)_\Omega + (4\ell_0^2 \nabla c, \nabla q)_\Omega = (1, q)_\Omega, \\ (\rho \mathbf{u}(0), \mathbf{w})_\Omega = (\rho \mathbf{u}_0, \mathbf{w})_\Omega, \\ (\rho \dot{\mathbf{u}}(0), \mathbf{w})_\Omega = (\rho \dot{\mathbf{u}}_0, \mathbf{w})_\Omega, \\ (c(0), q)_\Omega = (c_0, q)_\Omega. \end{cases} \quad (41)$$

where $(\cdot, \cdot)_\Omega$ is the \mathcal{L}_2 inner product on Ω .

3.2. The semidiscrete Galerkin form

Following the Galerkin method, we let $\mathcal{S}_t^h \subset \mathcal{S}_t$, $\mathcal{V}^h \subset \mathcal{V}$, $\tilde{\mathcal{S}}_t^h \subset \tilde{\mathcal{S}}_t$, and $\tilde{\mathcal{V}}^h \subset \tilde{\mathcal{V}}$ be the usual finite-dimensional approximations to the function spaces of the weak form (see [24] for details). The semi-discrete Galerkin form of the problem is then given as

$$(G) \begin{cases} \text{Given } \mathbf{g}, \mathbf{h}, \mathbf{u}_0, \dot{\mathbf{u}}_0, \text{ and } c_0 \text{ find } \mathbf{u}^h(t) \in \mathcal{S}_t^h \text{ and } c^h(t) \in \tilde{\mathcal{S}}_t^h, t \in [0, T], \text{ such that for all } \\ \mathbf{w}^h \in \mathcal{V}^h \text{ and for all } q^h \in \tilde{\mathcal{V}}^h, \\ (\rho \ddot{\mathbf{u}}^h, \mathbf{w}^h)_\Omega + (\boldsymbol{\sigma}, \nabla \mathbf{w}^h)_\Omega = (\mathbf{h}, \mathbf{w}^h)_{\partial\Omega_h}, \\ \left(\left(\frac{4\ell_0(1-k)\mathcal{H}}{\mathcal{G}_c} + 1 \right) c^h, q^h \right)_\Omega + (4\ell_0^2 \nabla c^h, \nabla q^h)_\Omega = (1, q^h)_\Omega, \\ (\rho \mathbf{u}^h(0), \mathbf{w}^h)_\Omega = (\rho \mathbf{u}_0, \mathbf{w}^h)_\Omega, \\ (\rho \dot{\mathbf{u}}^h(0), \mathbf{w}^h)_\Omega = (\rho \dot{\mathbf{u}}_0, \mathbf{w}^h)_\Omega, \\ (c^h(0), q^h)_\Omega = (c_0, q^h)_\Omega. \end{cases} \quad (42)$$

The explicit representations of \mathbf{u}^h , \mathbf{w}^h , c^h , and q^h in terms of the basis functions and nodal variables are

$$u_i^h = \sum_A^{n_b} N_A(\mathbf{x}) d_{iA}, \quad (43)$$

$$w_i^h = \sum_A^{n_b} N_A(\mathbf{x}) c_{iA}, \quad (44)$$

$$c^h = \sum_A^{n_b} N_A(\mathbf{x}) \phi_A, \quad (45)$$

$$q^h = \sum_A^{n_b} N_A(\mathbf{x}) \chi_A, \quad (46)$$

where n_b is the dimension of the discrete space, the N_A 's are the global basis functions, i is the spatial degree-of-freedom number, and d_{iA} , c_{iA} , ϕ_A , and χ_A are control variable degrees-of-freedom. Note that we have assumed that both the finite dimensional trial solution and weighting function spaces are defined by the same set of basis functions.

3.2.1. Isogeometric spatial discretization

In contrast to earlier work on phase-field models, we have chosen to use isogeometric spatial discretizations as introduced by Hughes et al. [25], which are based on NURBS and T-splines. T-splines are a generalization of NURBS that allows greater flexibility in geometric design including local refinement. A class of analysis-suitable T-splines was identified in [36,50]. This class of T-splines preserves the important mathematical properties of NURBS while providing an efficient and highly localized refinement capability. Analysis-suitable T-splines possess the following properties:

- Linear independence.
- The basis constitutes a partition of unity.
- Each basis function is non-negative.
- An affine transformation of an analysis-suitable T-spline is obtained by applying the transformation to the control points. We refer to this as affine covariance. This implies that all patch tests (see [24]) are satisfied *a priori*.
- They obey the convex hull property, see Piegl and Tiller [44].
- Local refinement is possible.

For additional details on basic T-spline analysis technology see Scott et al. [49].

The spline-based analysis strategy of isogeometric analysis has shown some advantages when compared to standard C^0 finite elements. First, isogeometric analysis allows for the efficient and exact geometric representation of many objects of engineering interest. Also, when using T-spline-based isogeometric analysis, efficient and automatic local mesh refinement strategies exist that preserve the exact geometry. Secondly, the isogeometric basis is in general smooth. Although the phase-field model permits the use of traditional C^0 finite elements, the use of a smooth base is anticipated to have favorable effects. One is that stresses are represented more accurately than with traditional C^0 finite elements, which has been observed to yield efficient spatial discretizations for discrete (see [52]) and smeared (see [53]) fracture models. Another study by Benson et al. [9] has shown that the accuracy of the spatial discretization of NURBS allows for more efficient time integration for explicit dynamics in the context of large deformation shells.

3.3. Time discretization and numerical implementation

3.3.1. Monolithic generalized- α time discretization

The monolithic time integration scheme is based on the generalized- α method introduced by Chung and Hulbert [18]. We define the residual vectors as

$$\mathbf{R}^u = \{\mathbf{R}_{A,i}^u\}, \quad (47)$$

$$\mathbf{R}_{A,i}^u = (\mathbf{h}, N_A \mathbf{e}_i)_{\partial\Omega_h} - (\rho \ddot{\mathbf{u}}^h, N_A \mathbf{e}_i)_\Omega - \left(\sigma_{jk}, B_{A,i}^{ijk} \right)_\Omega \quad (48)$$

and

$$\mathbf{R}^c = \{\mathbf{R}_A^c\}, \quad (49)$$

$$\mathbf{R}_A^c = (1, N_A)_\Omega - \left(\left(\frac{4\ell_0(1-k)\mathcal{H}}{\mathcal{G}_c} + 1 \right) c^h, N_A \right)_\Omega - \left(4\ell_0^2 \frac{\partial c^h}{\partial x_i}, \frac{\partial N_A}{\partial x_i} \right)_\Omega, \quad (50)$$

where \mathbf{e}_i is the i th Euclidean basis vector and

$$B_A^{ijk} = \frac{1}{2} \left(\frac{\partial N_A}{\partial x_j} \delta_{ik} + \frac{\partial N_A}{\partial x_k} \delta_{ij} \right) \quad (51)$$

so that $\varepsilon_{jk} = \sum_A B_A^{ijk} d_{A,i}$. For time step n , let \mathbf{d}_n and ϕ_n be the vectors of control variable degrees-of-freedom of the displacements and phase-field, respectively (see (43) and (45)). We then define $\mathbf{v}_n = \dot{\mathbf{d}}_n$, and $\mathbf{a}_n = \dot{\mathbf{d}}_n$. The monolithic generalized- α time integration scheme is then stated as follows: given $(\mathbf{d}_n, \mathbf{v}_n, \mathbf{a}_n)$, find $(\mathbf{d}_{n+1}, \mathbf{v}_{n+1}, \mathbf{a}_{n+1}, \mathbf{d}_{n+\alpha_f}, \mathbf{v}_{n+\alpha_f}, \mathbf{a}_{n+\alpha_m}, \phi_{n+1})$ such that

$$\mathbf{R}^u(\mathbf{d}_{n+\alpha_f}, \mathbf{v}_{n+\alpha_f}, \mathbf{a}_{n+\alpha_m}, \phi_{n+1}) = 0, \quad (52)$$

$$\mathbf{R}^c(\mathbf{d}_{n+\alpha_f}, \phi_{n+1}) = 0, \quad (53)$$

$$\mathbf{d}_{n+\alpha_f} = \mathbf{d}_n + \alpha_f(\mathbf{d}_{n+1} - \mathbf{d}_n), \quad (54)$$

$$\mathbf{v}_{n+\alpha_f} = \mathbf{v}_n + \alpha_f(\mathbf{v}_{n+1} - \mathbf{v}_n), \quad (55)$$

$$\mathbf{a}_{n+\alpha_m} = \mathbf{a}_n + \alpha_m(\mathbf{a}_{n+1} - \mathbf{a}_n), \quad (56)$$

$$\mathbf{v}_{n+1} = \mathbf{v}_n + \Delta t((1 - \gamma)\mathbf{a}_n + \gamma\mathbf{a}_{n+1}), \quad (57)$$

$$\mathbf{d}_{n+1} = \mathbf{d}_n + \Delta t \mathbf{v}_n + \frac{(\Delta t)^2}{2} ((1 - 2\beta)\mathbf{a}_n + 2\beta\mathbf{a}_{n+1}), \quad (58)$$

where $\Delta t = t_{n+1} - t_n$ is the time step and the parameters α_f , α_m , β , and γ define the method. These parameters will be discussed below.

At each time step, the solution is obtained using a Newton–Raphson method to solve the nonlinear equations above. Letting i be the Newton iteration, the residual vector and consistent tangent matrix for the linearized system are defined by

$$\frac{\partial \mathbf{R}_i^u}{\partial \mathbf{a}_{n+1}} \Delta \mathbf{a} + \frac{\partial \mathbf{R}_i^u}{\partial \phi_{n+1}} \Delta \phi = -\mathbf{R}_i^u, \quad (59)$$

$$\frac{\partial \mathbf{R}_i^c}{\partial \mathbf{a}_{n+1}} \Delta \mathbf{a} + \frac{\partial \mathbf{R}_i^c}{\partial \phi_{n+1}} \Delta \phi = -\mathbf{R}_i^c, \quad (60)$$

where

$$\mathbf{R}_i^u = \mathbf{R}^u(\mathbf{d}_{n+\alpha_f}^i, \mathbf{v}_{n+\alpha_f}^i, \mathbf{a}_{n+\alpha_m}^i, \phi_{n+1}), \quad (61)$$

and

$$\mathbf{R}_i^c = \mathbf{R}^c(\mathbf{d}_{n+\alpha_f}, \phi_{n+1}). \quad (62)$$

For each iteration, the linearized system defined by (59) and (60) is solved and iteration continues until convergence of the residual vectors occurs. For the examples discussed below, we have defined convergence as

$$\max \left\{ \frac{\|\mathbf{R}_i^u\|}{\|\mathbf{R}_0^u\|}, \frac{\|\mathbf{R}_i^c\|}{\|\mathbf{R}_0^c\|} \right\} \leq tol, \quad (63)$$

where $\|\cdot\|$ denotes the Euclidean norm. For the simulations considered in this work, $tol = 10^{-4}$ has been observed to be an appropriate choice.

3.3.1.1. Parameter selection. In [18] it was shown that α_f and α_m can be parametrized by the spectral radius, ρ_∞ , of the amplification matrix at $\Delta t = \infty$ such that second-order accuracy and unconditional stability are achieved for a second-order linear problem if

$$\alpha_f = \frac{1}{\rho_\infty + 1}, \quad (64)$$

$$\alpha_m = \frac{2 - \rho_\infty}{\rho_\infty + 1}, \quad (65)$$

$$\beta = \frac{1}{4}(1 + \alpha_m - \alpha_f)^2, \quad (66)$$

$$\gamma = \frac{1}{2} + \alpha_m - \alpha_f. \quad (67)$$

3.3.2. Staggered time discretization

For the staggered time integration scheme, we follow the general approach introduced by Larsen [34] where the momentum and phase-field equations are solved independently. At a given time step, the momentum equation is solved first to get the displacements. Using the updated displacements, the phase-field equation is solved. Larsen et al. [35] have shown existence and convergence results for this time discretization scheme.

In addition to reducing the problem to solving two smaller systems, this scheme also allows greater flexibility in how the momentum equation is solved, i.e., we can use either implicit or explicit schemes. For example, Bourdin et al. [15] studied the dynamic problem using backward difference in time to solve the momentum equation. Here, as with the monolithic scheme, we present algorithms that use α methods to solve the momentum equation. As with backward difference, the implicit α methods are stable. In contrast with backward difference, however, both implicit and explicit α methods provide second-order accuracy.

The staggered scheme can also be generalized to a predictor/multicorrector format where additional Newton–Raphson iterations can be performed within a time step. Below we present a general predictor/multicorrector algorithm, but for the results presented later we use only one pass of the corrector stage.

Defining the residual vectors for the momentum and phase-field equations by (48) and (50), and again letting \mathbf{d} and ϕ be arrays of the control variable coefficients in (43) and (45), the staggered predictor/multicorrector time integration scheme is stated as follows: given $(\mathbf{d}_n, \mathbf{v}_n, \mathbf{a}_n, \phi_n)$, solve

Predictor stage

$$i = 0 \quad (\text{iteration counter}), \quad (68)$$

$$\tilde{\mathbf{v}}_{n+1} = \mathbf{v}_n + \Delta t(1 - \gamma)\mathbf{a}_n, \quad (69)$$

$$\tilde{\mathbf{d}}_{n+1} = \mathbf{d}_n + \Delta t \mathbf{v}_n + \frac{(\Delta t)^2}{2} (1 - 2\beta)\mathbf{a}_n, \quad (70)$$

$$\mathbf{a}_{n+1}^{(i)} = 0, \quad (71)$$

$$\mathbf{v}_{n+1}^{(i)} = \tilde{\mathbf{v}}_{n+1}, \quad (72)$$

$$\mathbf{d}_{n+1}^{(i)} = \tilde{\mathbf{d}}_{n+1}, \quad (73)$$

$$\phi_{n+1}^{(i)} = \phi_n. \quad (74)$$

Multicorrector stage

$$\mathbf{a}_{n+\alpha_m}^{(i)} = \mathbf{a}_n + \alpha_m(\mathbf{a}_{n+1}^{(i)} - \mathbf{a}_n), \quad (75)$$

$$\mathbf{v}_{n+\alpha_f}^{(i)} = \mathbf{v}_n + \alpha_f(\mathbf{v}_{n+1}^{(i)} - \mathbf{v}_n), \quad (76)$$

$$\mathbf{d}_{n+\alpha_f}^{(i)} = \mathbf{d}_n + \alpha_f(\mathbf{d}_{n+1}^{(i)} - \mathbf{d}_n), \quad (77)$$

$$\mathbf{M}^* \Delta \mathbf{a} = \mathbf{R}^u(\mathbf{d}_{n+\alpha_f}^{(i)}, \mathbf{v}_{n+\alpha_f}^{(i)}, \mathbf{a}_{n+\alpha_m}^{(i)}, \phi_{n+1}^{(i)}), \quad (78)$$

$$\mathbf{a}_{n+1}^{(i+1)} = \mathbf{a}_{n+1}^{(i)} + \Delta \mathbf{a}, \quad (79)$$

$$\mathbf{v}_{n+1}^{(i+1)} = \tilde{\mathbf{v}}_{n+1} + \Delta t \gamma \mathbf{a}_{n+1}^{(i+1)}, \quad (80)$$

$$\mathbf{d}_{n+1}^{(i+1)} = \tilde{\mathbf{d}}_{n+1} + (\Delta t)^2 \beta \mathbf{a}_{n+1}^{(i+1)}, \quad (81)$$

$$\mathbf{K}^{cc} \Delta \phi = \mathbf{F}^c, \quad (82)$$

$$\phi_{n+1}^{(i+1)} = \Delta \phi. \quad (83)$$

The phase-field arrays in (82) are defined as

$$\mathbf{K}^{cc} = [K_{AB}], \quad (84)$$

$$K_{AB} = \left(\left(\frac{4\ell_0(1-k)\mathcal{H}}{\mathcal{G}_c} + 1 \right) N_B, N_A \right)_\Omega + \left(4\ell_0^2 \frac{\partial N_B}{\partial x_i}, \frac{\partial N_A}{\partial x_i} \right)_\Omega, \quad (85)$$

$$\mathbf{F}^c = \{F_A\}, \quad (86)$$

$$F_A = (1, N_A), \quad (87)$$

and $\Delta t = t_{n+1} - t_n$ is the time step and the parameters α_m , α_f , β , and γ , which define the method, are selected as described below.

If the linearized momentum Eq. (78) is being solved implicitly then

$$\mathbf{M}^* = -\frac{\partial \mathbf{R}_i^u}{\partial \mathbf{a}_{n+1}} = \alpha_m \mathbf{M} + \alpha_f \beta (\Delta t)^2 \mathbf{K}, \quad (88)$$

where \mathbf{M} is the consistent mass matrix and

$$\mathbf{K} = [K_{AB,ij}^{uu}], \quad (89)$$

$$K_{AB,ij}^{uu} = \left(\frac{\partial \sigma_{lk}}{\partial \varepsilon_{mn}} B_B^{jmn}, B_A^{ilk} \right)_\Omega \quad (90)$$

is the consistent damage-elastic tangent stiffness matrix. If we let $\mathbf{M}^* = \alpha_m \tilde{\mathbf{M}}$ where $\tilde{\mathbf{M}}$ is the lumped mass matrix then the linearized momentum equation is solved explicitly. When computing with NURBS and T-splines, we compute $\tilde{\mathbf{M}}$ using the row-sum technique as described in [24]. Due to the fact that NURBS and T-spline basis functions are point-wise positive, the row-sum lumped mass matrix is guaranteed to be positive. Furthermore, it is also mass conservative.

3.3.2.1. Parameter selection. For the staggered solution strategy, the choice of α_m , α_f , and \mathbf{M}^* provides several options for the type of algorithm that is used to solve the linear momentum problem. For the fully implicit case ($\mathbf{M}^* = \alpha_m \mathbf{M} + \alpha_f \beta (\Delta t)^2 \mathbf{K}$) we use the generalized- α method described above. For the fully explicit case ($\mathbf{M}^* = \alpha_m \mathbf{M}$) we use either the HHT- α of Hilber et al. [23] or the explicit generalized- α method of Hulbert and Chung [28]. The HHT- α method, parameterized by α , provides a second-order accurate family of algorithms for linear second-order equations if $\alpha \in [-\frac{1}{3}, 0]$ and

$$\alpha_m = 1, \quad (91)$$

$$\alpha_f = 1 + \alpha, \quad (92)$$

$$\beta = \frac{(1 - \alpha)^2}{4}, \quad (93)$$

$$\gamma = \frac{1 - 2\alpha}{2} \quad (94)$$

(see [39]). The explicit generalized- α method, as shown by Hulbert and Chung [28], is a one-parameter family of explicit algorithms that provides optimal numerical dissipation and is second-order accurate for linear problems if $\alpha_f = 0$ and

$$\alpha_m = \frac{2 - \rho_b}{1 + \rho_b}, \quad (95)$$

$$\beta = \frac{5 - 3\rho_b}{(1 + \rho_b)^2 (2 - \rho_b)}, \quad (96)$$

$$\gamma = \alpha_m + \frac{1}{2}, \quad (97)$$

where ρ_b is the spectral radius value at the bifurcation limit of the principal roots of the characteristic equation.

4. Numerical results

In this section we investigate the numerical performance of the phase-field fracture model. All geometries have been discretized spatially using either NURBS or T-spline basis functions (which we refer to as the global smooth basis). The numerical computation for all the models was performed using the Bézier extraction methods described by Borden et al. [10] and Scott et al. [49]. Bézier extraction constructs the minimal set of Bézier elements defining a NURBS or T-spline. A Bézier element is a region of the physical domain in which the basis functions are C^∞ -continuous and over which integration is performed. In addition to defining elements, Bézier extraction also builds an extraction operator for each Bézier element that maps a Bernstein polynomial basis defined on the Bézier element to the global smooth basis. The transpose of the

extraction operator maps the control points of the global smooth basis to the Bézier control points. The idea is illustrated in Fig. 4 for a cubic B-spline curve. The B-spline curve with its control points, $\mathbf{P} = \{\mathbf{P}_i\}_{i=1}^7$, and basis functions, $\mathbf{N} = \{\mathbf{N}_i\}_{i=1}^7$, is shown on the left with the elements, Ω_e , defined on the parametric domain. On the right we illustrate the action of the extraction operator, $\mathbf{C}_2 \in \mathbb{R}^{4 \times 4}$, for Ω_2 . The transpose of the extraction operator, \mathbf{C}_2^T , defines the Bézier control points, $\mathbf{Q}_2 = \{\mathbf{Q}_{2,i}\}_{i=1}^4$, for the Bézier element in terms of the global control points, as shown in Fig. 4. The Bernstein polynomial basis functions, $\mathbf{B} = \{\mathbf{B}_i\}_{i=1}^4$, are shown below the Bézier element. The extraction operator is used to extract the smooth B-spline basis functions $\mathbf{N}_2 = \{\mathbf{N}_i\}_{i=2}^5$ from the Bernstein basis, i.e., the B-spline basis functions can be written as linear combinations of the Bernstein basis functions. Bézier extraction provides a completely local representation of the global smooth basis. It provides an element data structure that can be integrated into existing finite element frameworks in a straightforward manner.

To integrate arrays over the Bézier elements we use Gaussian quadrature with a $p + 1$ rule in each parametric direction, where p is the polynomial degree of the basis functions. Thus, in two-dimensions we use a 3-by-3 quadrature rule for quadratic basis functions and a 4-by-4 quadrature rule for cubic basis functions. Hughes et al. [27] have shown that smooth bases allow for more efficient quadrature rules. See also the appendix in [26] which demonstrates the stability and accuracy of reduced quadrature rules for NURBS. This is beyond the scope of the work presented here and we acknowledge that the quadrature rules we use may represent overkill.

For the examples below, the reported mesh sizes, h , are computed on the Bézier elements as $h = \sqrt[3]{a}$ where a is the area of an element in two dimensions and the volume of an element in three dimensions and d is the number of spatial dimensions. In most cases, the mesh is such that $h = \ell_0/2$ in the area where a crack has formed. Experience has shown that this relationship between h and ℓ_0 provides sufficient accuracy without over resolving the crack.

4.1. 2D quasi-static shear load

In this section we consider a displacement-controlled quasi-static benchmark test from Miehe et al. [37] in order to compare the results obtained from standard C^0 finite elements and isogeometric finite elements. The geometry and boundary conditions of the model are shown in Fig. 5. We use C^2 -continuous cubic T-splines for the spatial discretization of the model and the staggered quasi-static solution strategy described by Miehe et al. [37] to obtain the solution at each displacement increment. As can be seen from Fig. 5b, T-splines can be locally refined in the area where the crack forms. This is in contrast to a NURBS, where refinement propagates globally to produce a much denser mesh.

The material parameters are $E = 210$ GPa, $\nu = 0.3$, and $G_c = 2700$ J/m² and plane strain is assumed. The length scale is chosen to be $\ell_0 = 7.5 \times 10^{-6}$ m and we do not include a viscous damping term on the phase-field. The T-spline was refined *a priori* based on the expected solution. The initial crack is modeled as a discrete discontinuity in the geometry and the T-spline contains C^0 lines that radiate out from the crack tip so that the mesh is divided into four equal square subdomains of C^2 continuity. These C^0 lines were included to facilitate modeling the sharp crack tip as a C^0 geometric feature. An alternative would have been to use a globally C^2 -continuous T-spline on the entire domain and to introduce the crack through an induced crack in the phase-field (see Appendix A). The locally refined T-spline contained 5587 cubic basis functions. The calculations of Miehe et al. [37] utilized 30,000 linear triangles.

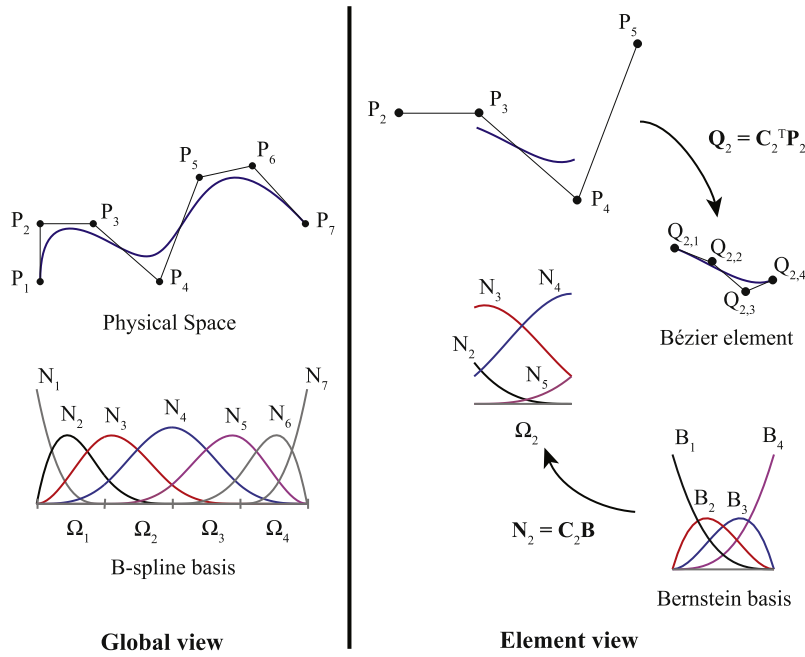


Fig. 4. Bézier extraction for a cubic B-spline curve. The B-spline curve and basis functions are shown on the left. The action of the extraction operator, \mathbf{C}_2 , for element Ω_2 is illustrated on the right. The transpose of the extraction operator defines the control points, $\mathbf{Q}_2 = \{\mathbf{Q}_{2,i}\}_{i=1}^4$, of the Bézier element from the control points, $\mathbf{P}_2 = \{\mathbf{P}_i\}_{i=2}^5$ of the B-spline curve. The B-spline basis functions, $\mathbf{N}_2 = \{N_i\}_{i=2}^5$, can be computed over the element by applying the extraction operator to Bernstein polynomial basis functions, $\mathbf{B} = \{B_i\}_{i=1}^4$, defined on the Bézier element. Note that the Bernstein basis is the same for each element. Formation of element arrays can thus be standardized in a shape function routine.

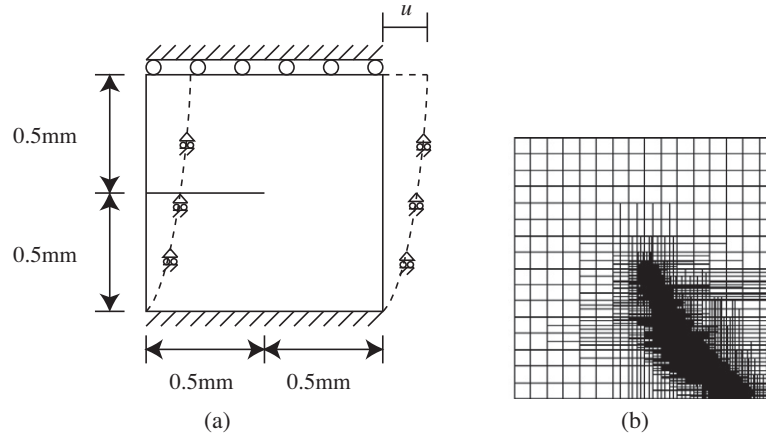


Fig. 5. Input model for the quasi-static shear benchmark test: (a) geometry and boundary conditions and (b) the Bézier element representation of the T-spline. The T-spline contains 5587 cubic basis functions and the effective element size is between $h_{\min} = 3.906 \times 10^{-3}$ mm and $h_{\max} = 6.25 \times 10^{-2}$ mm. The refinement was performed *a priori* based on knowledge of the expected crack path.

Fig. 6 shows the progression of the crack at several load levels and the load–displacement curve is shown in Fig. 7 with a comparison to the results reported by Miehe et al. [37]. As can be seen from the load–displacement curve, the results obtained from the T-spline mesh are in good agreement with those obtained from standard C^0 finite elements, but with far fewer degrees-of-freedom. We attribute this to the smooth description of the stress fields, which was also observed to be beneficial in cohesive zone modeling by Verhoosel et al. [52] and gradient damage modeling by Verhoosel et al. [53].

4.2. Dynamic crack branching

In this example, we model a pre-notched rectangular plate loaded dynamically in tension. The geometry and boundary conditions of the problem are shown in Fig. 8. A traction load is applied

to the top and bottom surface at the initial time step and held constant throughout the simulation. All other surfaces have a zero traction condition applied. This load condition is such that crack branching will occur (see [51] for a report of results for this problem using several other methods of dynamic fracture analysis). The initial crack is induced by an initial strain-history field (see Appendix A) allowing the geometry to be modeled as a continuous quadratic C^1 -continuous NURBS patch.

The model parameters are $\rho = 2450$ kg/m³, $E = 32$ GPa, $\nu = 0.2$, $\mathcal{G}_c = 3$ J/m², and plane strain is assumed. The corresponding dilatational, shear, and Rayleigh wave speeds are $v_d = 3810$ m/s, $v_s = 2333$ m/s, $v_R = 2125$ m/s. The length scale was chosen to be $\ell_0 = 2.5 \times 10^{-4}$ m. The monolithic generalized- α time integration scheme discussed in Section 3.3.1 was used with $\rho_\infty = 0.5$.

Table 1 lists the parameters for three successively finer meshes used for this example. A uniform mesh was used to remove any

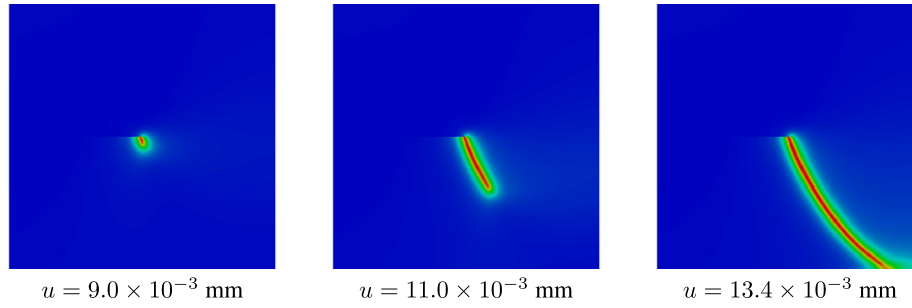


Fig. 6. Crack progression for the quasi-static shear test at several load increments.

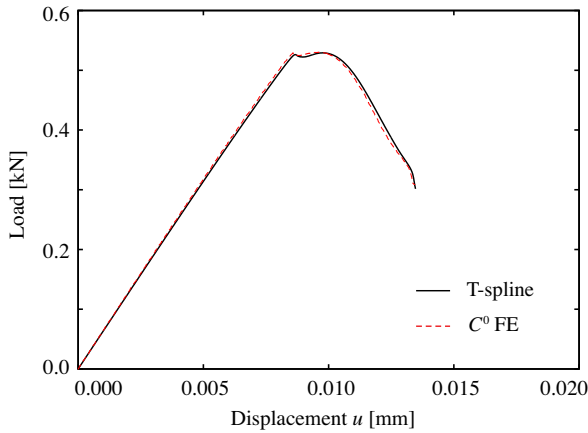


Fig. 7. Force-displacement curve for the quasi-static shear test. The results obtained using the T-spline discretization are compared to those reported by Miehe et al. [37] using standard C^0 finite elements.

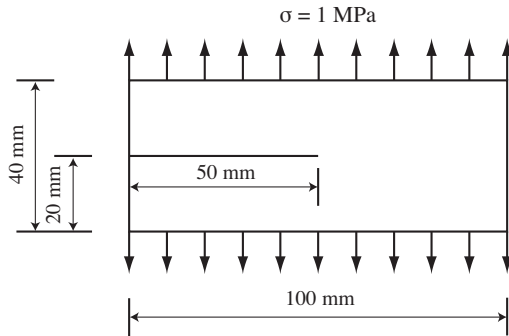


Fig. 8. The geometry and boundary conditions for the crack branching example. In the simulation the initial crack is modeled by introducing an initial strain history field that induces a phase field at the initial crack location, and the geometry and displacement field are C^1 continuous throughout (see Appendix A).

effect from mesh distribution and size variation. To ensure accurate results, the time step was chosen for each mesh such that $\Delta t \approx h/v_R$.

In order to make a comparison between the results from the three meshes we define the elastic strain energy as

Table 1

The mesh sizes and time steps used for the dynamic crack branching example. The mesh is a uniform, quadratic NURBS in each case. To ensure accurate results, the time step size is chosen to be roughly h/v_R .

	h (m)	Δt (s)
Mesh 1	2.5×10^{-4}	1×10^{-7}
Mesh 2	1.25×10^{-4}	5×10^{-8}
Mesh 3	6.25×10^{-5}	2.5×10^{-8}

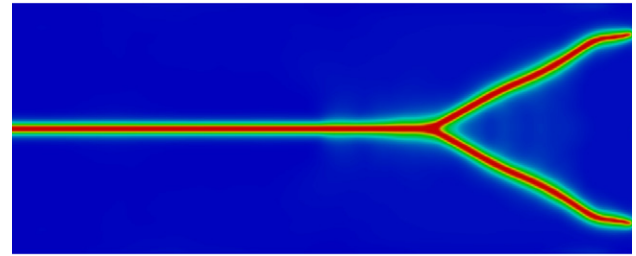
$$\mathcal{E}_e = \int_{\Omega} \{[(1-k)c^2 + k]\psi_e^+(\boldsymbol{\varepsilon}) + \psi_e^-(\boldsymbol{\varepsilon})\} d\mathbf{x} \quad (98)$$

and the dissipated energy as

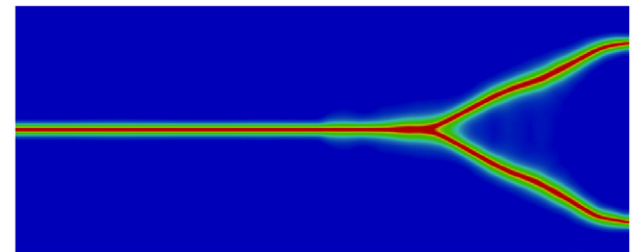
$$\mathcal{E}_d = \int_{\Omega} \mathcal{G}_c \left[\frac{(c-1)^2}{4\ell_0} + \ell_0 \frac{\partial c}{\partial x_i} \frac{\partial c}{\partial x_i} \right] d\mathbf{x}. \quad (99)$$

These values provide a measure of the global response of the model.

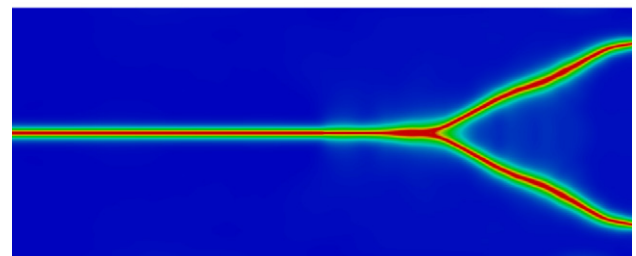
The final phase-field results for each mesh are shown in Fig. 9. As can be seen, the crack path is similar for all meshes although mesh 1 ($h = \ell_0$) fails to reach the boundary in the same amount of time as the other two. This is typical of the behavior seen when the mesh is too coarse to adequately resolve the phase-field transition near the crack. Coarse meshes tend to limit the crack tip



(a) Mesh 1 with $h = 2.5 \times 10^{-4}$ m



(b) Mesh 2 with $h = 1.25 \times 10^{-4}$ m



(c) Mesh 3 with $h = 6.25 \times 10^{-5}$ m

Fig. 9. Results for the crack branching example at $t = 80 \mu s$. For all three meshes $\ell_0 = 2.5 \times 10^{-4}$ m.

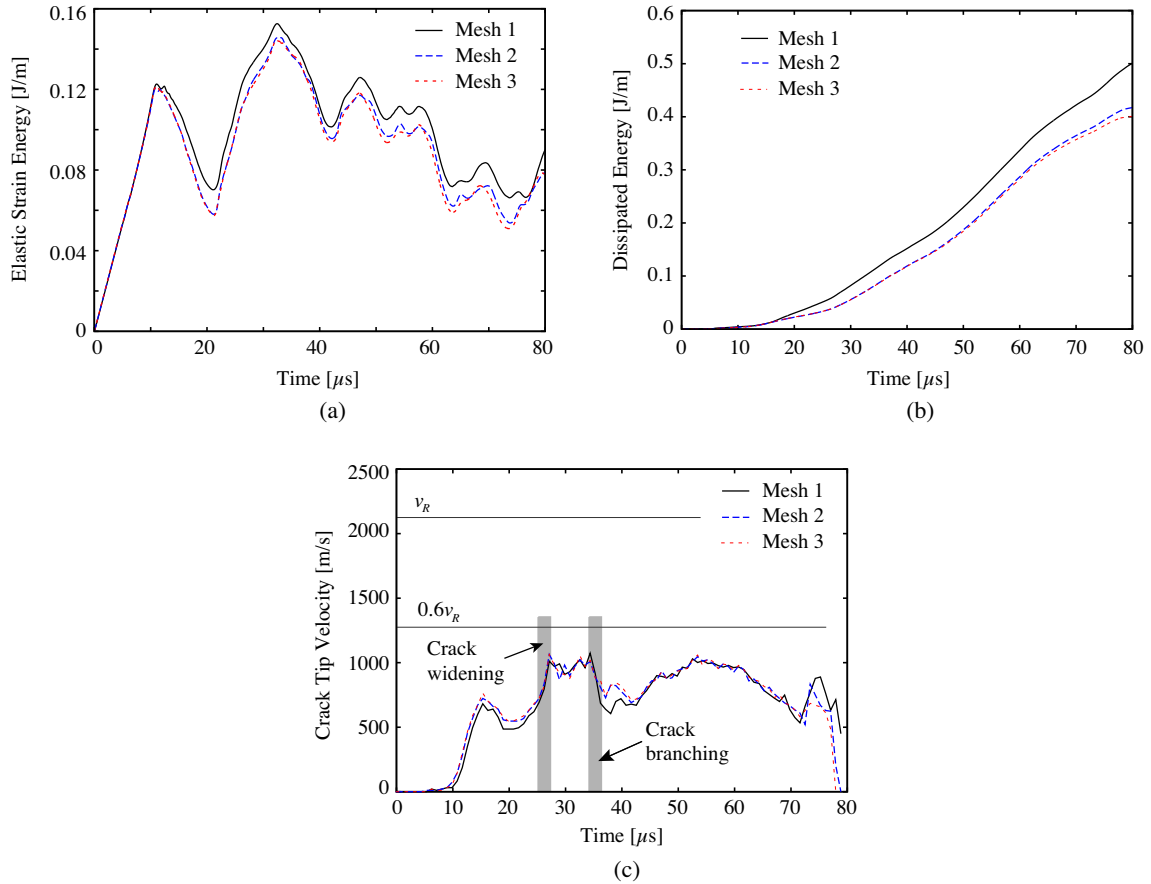


Fig. 10. Plots over time of (a) the elastic strain energy per unit thickness, as defined by (98), (b) the dissipated fracture energy per unit thickness, as defined by (99), and (c) crack tip velocity. After branching, the reported crack tip velocity is that of the upper branch. In (c), the terminology “crack widening” refers to the broadening of the damage zone prior to branching. It may be considered something between incipient branching and a precursor to branching. For finite ℓ_0 , it is not possible to say precisely where branching begins.

velocity. It is difficult to see a difference in the crack path between mesh 2 and mesh 3.

Fig. 10(a) shows the elastic strain energy as defined by (98) and Fig. 10(b) show the energy dissipated by the formation of the crack as defined by (99). These plots show that $h = \ell_0/2$ provides enough resolution to capture the response of the model. We note the dissipated energy is overestimated for mesh 1 by about 25% compared with the converged results, which is consistent with the estimate emanating from the Γ -convergence proof of Bourdin, Francfort, and Marigo [14], that is, a factor of $h/4\ell_0$. However, this estimate appears to be a bit pessimistic compared with the numerical results obtained for mesh 2 and 3. This might be expected given the conservative nature of convergence analyses of this type. The crack tip velocity is plotted in Fig. 10(c). In all cases, the velocity

stays well below 60% of the Rayleigh wave speed as has been commonly observed in experiments (see [46]).

In Fig. 11 we show a post-processed plot of mesh 2 at $t = 70 \mu s$. In this figure we have scaled the displacements by a factor of 50 and removed areas of the model from the plot where $c < 0.05$ in order to show a representation of the cracked geometry.

Remark 4.1. For the monolithic time integration scheme the size of Δt is limited by accuracy and convergence. For the dynamic crack branching example discussed here, choosing a time step such that $\Delta t \leq 2h/v_R$ produced acceptable accuracy. For $\Delta t = 8h/v_R$ the Newton–Raphson method failed to converge near the time of the initial crack propagation.

Remark 4.2. The simulation was repeated for mesh 2 using the staggered algorithm described in Section 3.3.2 and solving the momentum equation implicitly while all other parameters were kept the same as listed above. The results were similar, but slightly different. Specifically, the results for the elastic strain energy were between the results for meshes 1 and 2 in Fig. 10(a), whereas the results for dissipated energy were essentially the same as for mesh 2 in Fig. 10(b).

Remark 4.3. Since the crack is not tracked algorithmically, the velocity of the crack tip is measured as a post-processing step. For the values reported here, the location of the crack tip, x , is found on an iso-curve of the phase-field with value 0.25. The velocity is then computed as $v_n = (x_{n+1} - x_n)/\Delta t$.

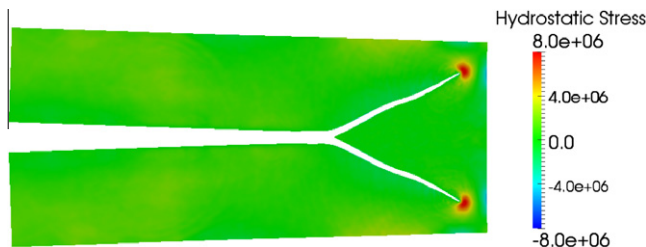


Fig. 11. A post-processed plot of mesh 2 at $t = 70 \mu s$. The displacements have been scaled by a factor of 50 and areas of model where $c < 0.05$ have been removed from the plot. Hydrostatic stress is measured in Pascals.

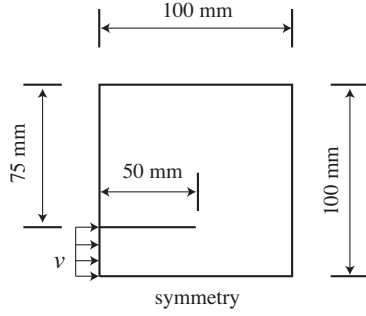


Fig. 12. The geometry and boundary conditions for the dynamic shear loading example. The crack is modeled by an actual discontinuity in the mesh with a zero radius crack tip. The load is applied as a velocity condition that is ramped up from 0 to 16.5 m/s in one microsecond and then held constant for the duration of the simulation.

4.3. Dynamic shear loading

In this example we model crack initiation and propagation under a dynamic shear load. The model is based on experimental results reported by Kalthoff and Winkler [30] and Kalthoff [29]. Previous numerical results of this problem based on XFEM have been reported by Belytschko et al. [6], among others, and a comparison of results between XFEM, the element deletion method, and the interelement crack method have been reported by Song

et al. [51]. Numerical results of a similar experiment reported by Ravi-Chandar [45] have been reported by Remmers et al. [48] where cohesive segments have been used to model the crack.

The input geometry and loading conditions for the simulation are shown in Fig. 12, where symmetry is employed to reduce the computational cost. In the experiment, the load was applied by firing a projectile at a prenotched specimen. In our simulation we model the case where the projectile was fired with a velocity of 33 m/s by applying the kinematic velocity

$$v = \begin{cases} \frac{t}{t_0} v_0 & t \leq t_0, \\ v_0 & t > t_0, \end{cases} \quad (100)$$

where $v_0 = 16.5$ m/s and $t_0 = 1$ μ s. A no traction boundary condition is applied to all unspecified surfaces. We model the geometry using quadratic NURBS basis functions. The initial crack is modeled by a discontinuity in the geometry in order to introduce a sharp crack tip as in Section 4.1.

The model parameters are $\rho = 8000$ kg/m³, $E = 190$ GPa, $\nu = 0.3$, $G_c = 2.213 \times 10^4$ J/m², $k = 0$, and plane strain is assumed. The corresponding dilatational, shear, and Rayleigh wave speeds are $v_d = 5654$ m/s, $v_s = 3022$ m/s, $v_R = 2803$ m/s. The length scale was chosen to be $\ell_0 = 1.95 \times 10^{-4}$ m leading to a maximum uniaxial stress of 1.07 GPa (see Section 2.3.1). The mesh has 1024×1024 uniform quadratic elements so that $h \approx \ell_0/2$.

The simulations were performed using the staggered integration scheme described in Section 3.3.2 with the momentum equation being solved explicitly using the HHT- α method with $\alpha = -0.1$. A

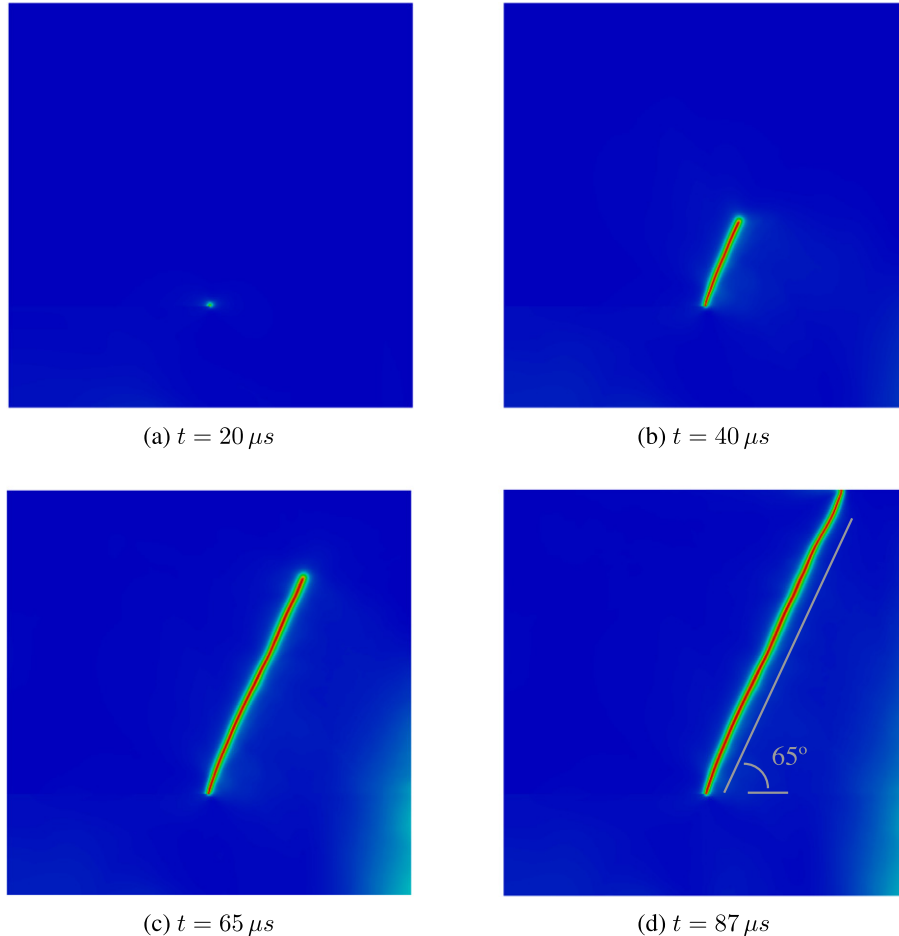


Fig. 13. Evolution of the crack through time for a uniform 1024×1024 quadratic NURBS mesh with 1,055,242 control points and $\ell_0 = 1.95 \times 10^{-4}$ m. The resulting crack propagation angle is somewhat greater than 65° and close to the experimentally observed angle of about 70° reported by Kalthoff and Winkler [30] and Kalthoff [29].

fixed time step of $\Delta t = 1.25 \times 10^{-8}$ was chosen, which is slightly less than $0.9\Delta t_{crit}$, where the critical time step, Δt_{crit} , is computed as

$$\Delta t_{crit} = \frac{\Omega_{crit}}{\omega_{max}} \quad (101)$$

with ω_{max} the maximum natural frequency of the momentum equation determined from the undamped eigenproblem and (considering only the undamped case).

HHT- α (see [39])

$$\Omega_{crit} = \frac{\sqrt{2(\gamma + 2\alpha(\gamma - \beta))}}{\gamma + 2\alpha(\gamma - \beta)}. \quad (102)$$

Explicit generalized- α (see [28])

$$\Omega_{crit} = \sqrt{\frac{12(1 + \rho_b)^3(2 - \rho_b)}{10 + 15\rho_b - \rho_b^2 + \rho_b^3 - \rho_b^4}}. \quad (103)$$

The resulting phase-field is shown in Fig. 13. Note that, initially, the crack starts to propagate at a larger angle then the angle decreases as the crack propagates. The average angle from the initial crack tip to the point where the crack intersects the boundary is somewhat greater than 65° . This is in fairly good agreement with the experimental results, which show the crack propagating at about 70° . The velocity of the crack tip is shown in Fig. 15. As can be seen, the crack quickly accelerates to a velocity just below 60% of the Rayleigh wave speed and maintains this velocity until it decreases as the crack approaches the top surface. Although no crack tip velocity information is reported for the experimental results, this velocity behavior is in good agreement with behavior reported by Ravi-Chandar [45] for a similar experiment.

In Fig. 14 we show a post-processed plot of the model at $t = 70\mu s$. In this figure we have scaled the displacements by a factor of 5 and removed areas of the model from the plot where $c < 0.05$ in order to show a representation of the cracked geometry.

Remark 4.4. Experience has shown that the action of the phase-field does not effect the critical time step of the explicit algorithm. Choosing $\Delta t \leq 0.9\Delta t_{crit}$ has proven sufficient to maintain stability and is often conservative, i.e., letting $\Delta t = \Delta t_{crit}$ often results in a stable time step.

4.4. Adaptive refinement scheme

The length scale parameter, ℓ_0 , plays two roles in the phase-field model: first, it determines the width of the approximation to the crack, and second, as shown in Section 2.3.1, it influences the magnitude of the tensile stress required for crack nucleation. Thus, in order to capture fine scale details of a crack, or model materials with high nucleation stresses, a small value for ℓ_0 is needed. For example, if the maximum uniaxial shear stress is too low for the dynamic shear loading example in Section 4.3, a secondary crack

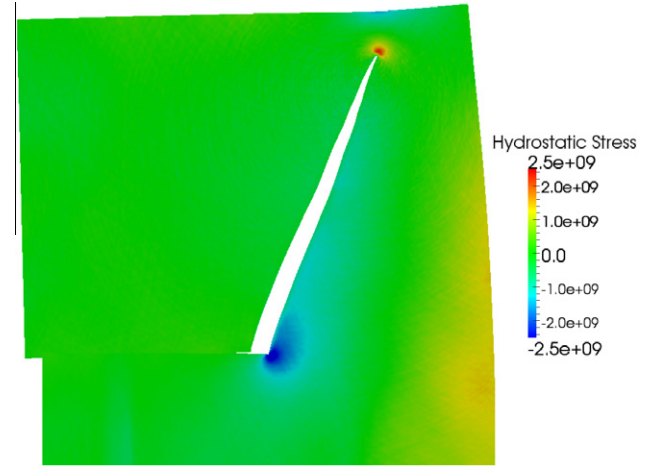


Fig. 14. A post-processed plot of the dynamic shear loading example at $t = 75\mu s$. The displacements have been scaled by a factor of 5 and areas of model where $c < 0.05$ have been removed from the plot. Pressure is measured in Pascals.

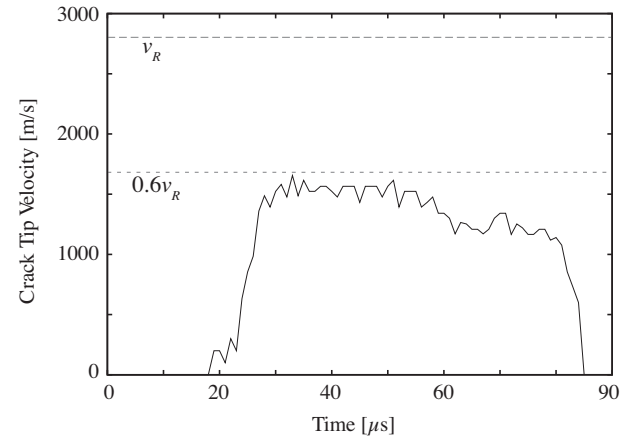


Fig. 15. Crack tip velocity for dynamic shear loading example.

will nucleate at the surface opposite the initial crack (see [47]). Thus, a small value of ℓ_0 is required to accurately capture the crack topology for this problem. This in turn requires a fine mesh in areas where the crack is located.

To efficiently compute with fine meshes, as needed to accurately resolve a crack for small values of ℓ_0 , we introduce an adaptive refinement scheme. For this scheme we choose the phase-field parameter as a convenient measure for determining the need for refinement. As has been shown, the gradients of the phase-field are high in an area near the crack. Away from the crack the value of the phase-field stays close to one. By choosing a critical threshold of the phase-field that is higher than the value at which crack nucleation occurs ($c = 0.75$) the area near the crack is easily

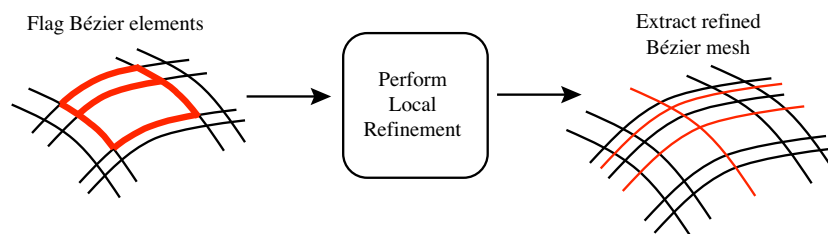


Fig. 16. A schematic representation of an adaptive refinement scheme based on T-splines, analysis-suitable local refinement, and Bézier extraction.

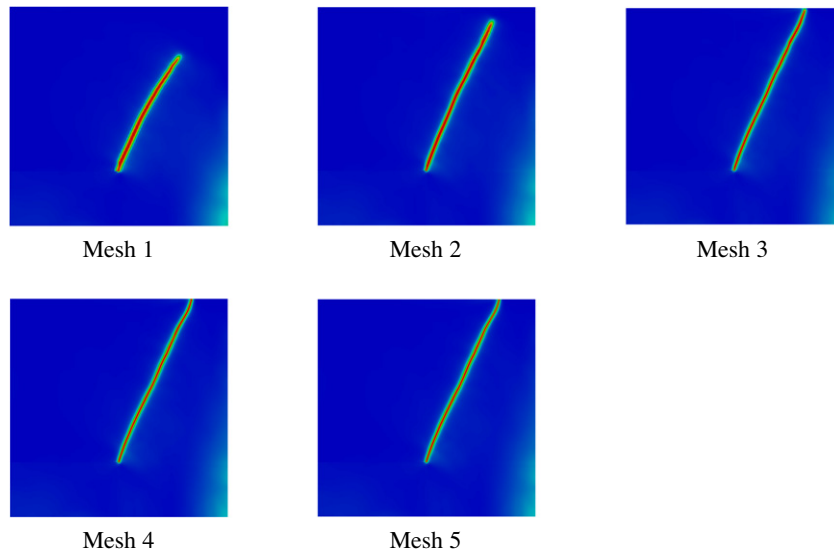


Fig. 17. Kalthoff mesh refinement results. Mesh 1 is a 128×128 cubic T-spline mesh. Bézier elements were flagged for refinement if $c < 0.8$ at any quadrature point inside the element and $h = \sqrt{a} > 1.94 \times 10^{-4}$ m where a is the element area.

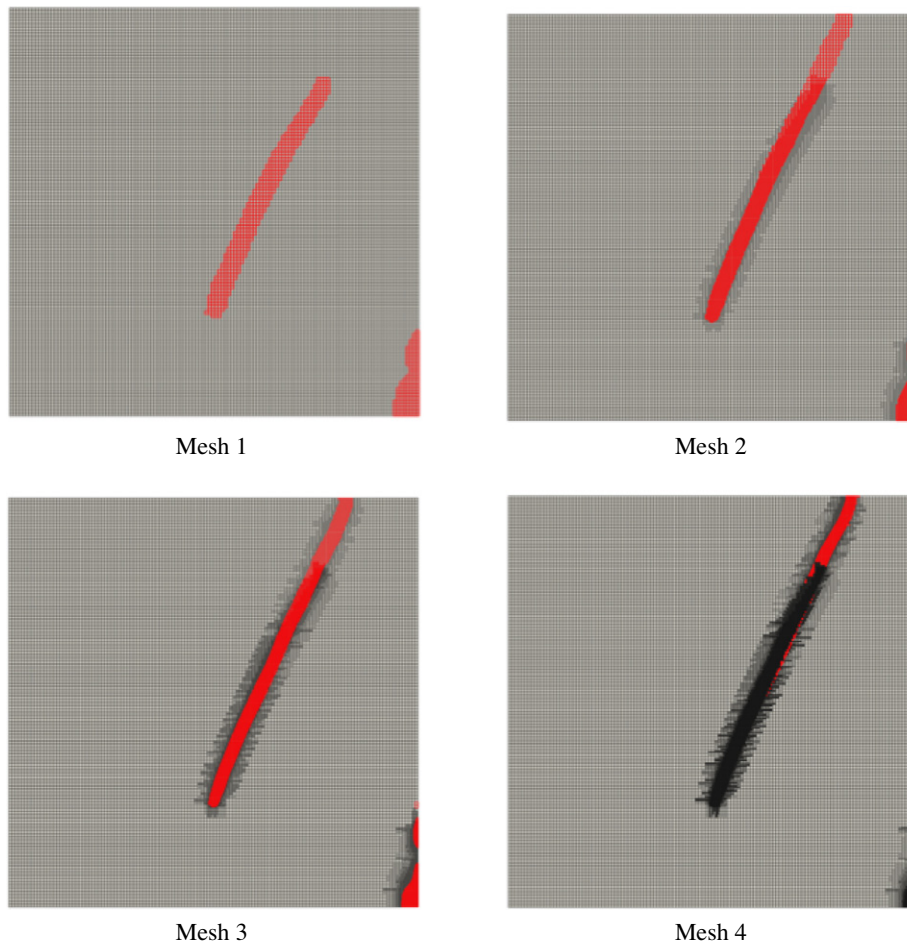


Fig. 18. The first four meshes in the local refinement sequence. The elements in red are those that were selected to be refined at each step. (For interpretation of the references to color in this figure legend, the reader is referred to the web version of this article.)

identified. Using a larger value for the critical threshold results in a greater area of refinement (we have found $c = 0.8$ to be a good

choice). The adaptive refinement scheme we have developed proceeds as follows:

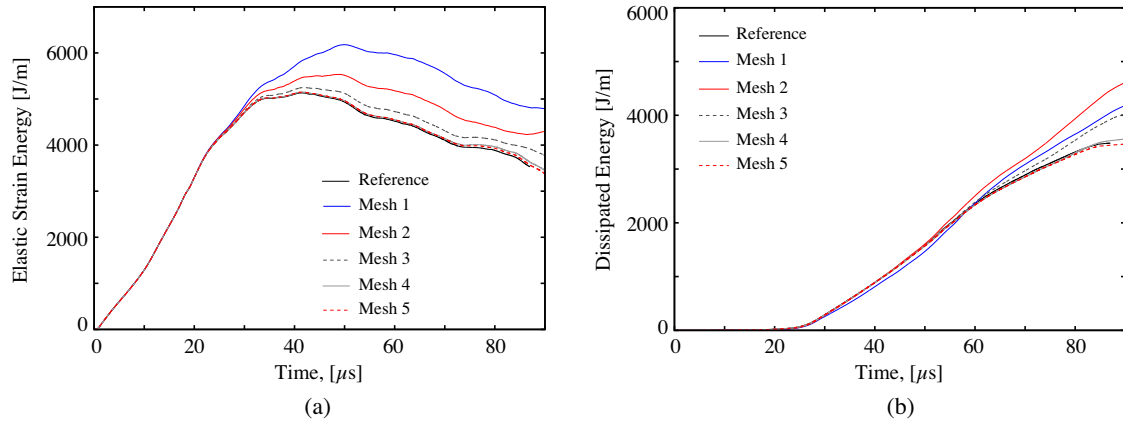


Fig. 19. The (a) elastic strain energy, $\int_{\Omega} \{[(1-k)c^2 + k]\psi_e^+ + \psi_e^-\} d\mathbf{x}$, per unit thickness and (b) dissipated energy, $\int_{\Omega} \mathcal{G}_c [(c-1)^2/(4\ell_0) + \ell_0 |\nabla c|^2] d\mathbf{x}$, per unit thickness for the sequence of refined meshes shown in Fig. 17. The reference mesh is the uniformly refined mesh from Fig. 13.

1. Run the dynamic simulation to some termination point.
2. Flag elements where the phase-field is below the critical threshold.
3. Refine the flagged elements.
4. Rerun the simulation with the locally refined mesh.
5. Repeat steps 2–4 until convergence.

4.4.1. Analysis-suitable local refinement of T-splines

A distinguishing feature of T-splines is the presence of T-junctions (hanging nodes) in the mesh. T-junctions maintain locality in the context of refinement. This is in contrast with NURBS where all refinement is global. A highly localized and efficient refinement algorithm for analysis-suitable T-splines was developed by Scott et al. [50]. This algorithm avoids introducing superfluous control points, preserves exact geometry, generates smooth nested spaces, and maintains the properties of an analysis-suitable space.

In the context of isogeometric analysis, the adaptive refinement scheme is based on Bézier extraction and analysis-suitable local refinement as shown schematically in Fig. 16. First, the flagged Bézier elements are used to determine the basis functions of the T-spline that will be refined. Analysis-suitable local refinement is then applied to generate the refined set of T-spline basis functions. Bézier extraction is then applied to the refined T-spline to generate the new set of Bézier elements.

We apply this refinement scheme to the dynamic shear loading example from Section 4.3. We start with a coarse initial C^2 -continuous cubic T-spline that has 128×128 Bézier elements. For all meshes, ℓ_0 is set to 1.95×10^{-4} m. Elements are flagged for refinement if the phase-field parameter is less than 0.8 at any quadrature point within the element. The sequence of results shown in Fig. 17 where each simulation was terminated at $t = 100 \mu\text{s}$. Fig. 18 shows the sequence of meshes with the elements that have been flagged for refinement at the end of each iteration. Note that when the mesh is too coarse, the crack propagation is restricted and the direction is incorrect. It is not until mesh 3, when $h = \ell_0$, that the mesh is fine enough to capture the correct crack path.

Fig. 19 compares the elastic strain energy and dissipated energy at each refinement iteration to the solution from Section 4.3, which we call the reference solution. The elastic strain energy, shown in Fig. 19(a), is over predicted for the coarse meshes as a result of restricted crack propagation. This plot shows that it is not until mesh 4, when most of the element along the propagation path are such that $h = \ell_0/2$, that the elastic strain energy agrees well with the reference solution. This is also true for the dissipated energy shown in Fig. 19(b).

Table 2

The number of basis functions before refinement and the number of elements that were flagged for refinement for each mesh.

	Mesh 1	Mesh 2	Mesh 3	Mesh 4	Mesh 5
Number of functions	17,755	19,992	27,032	47,824	53,032
Flagged elements	589	2001	6257	1446	8

Table 2 lists the total number of functions for each mesh in the refinement sequence and the number of elements that were flagged at the end of each simulation. Note that the final mesh has 53,032 cubic basis functions. This is compared to 1,055,242 quadratic basis functions in the uniformly refined reference solution from Section 4.3.

Remark 4.5. A straight crack propagating at 65° from the initial crack tip would have a total length of about 8.3×10^{-2} m. Given $\mathcal{G}_c = 2.213 \times 10^4$ J/m², this would lead to a surface energy of approximately 1837 J. The final dissipated energy reported in Fig. 19(b) is approximately 3500 J, or just less than twice the value expected given the length of the crack. Irreversibility (*i.e.*, the use of \mathcal{H}) seems to play a role here, but one that we do not currently fully understand. When we remove \mathcal{H} and let the crack heal upon closure, the computed dissipated energy is still overestimated by about 40%. Additionally, the threshold in the phase-field equation for accumulating damage is zero, *i.e.*, c is less than one as soon as ψ_e^+ is greater than zero. This is probably unrealistic, especially in a dynamics problem in which tensile waves are propagating throughout the domain. Even in the case when irreversibility is not enforced this will contribute to the dissipated energy calculation. We feel this unphysical footprint of damage can be addressed by a more realistic threshold as is commonly used in damage theories.

4.5. Pressurized cylinder with solid elements

A major benefit of the phase-field formulation presented here is that it extends easily to three dimensions. As a final example, we show a three-dimensional computation of a pressurized cylinder with a spherical end cap. The input geometry for the simulation is shown in Fig. 20 where symmetry is used to reduce the computational cost. The initial crack is modeled by an induced phase-field (see Appendix A). A linearly increasing hydrostatic pressure load, p , is applied to the inner surface as $p = 50t$ MPa where t is the current time.

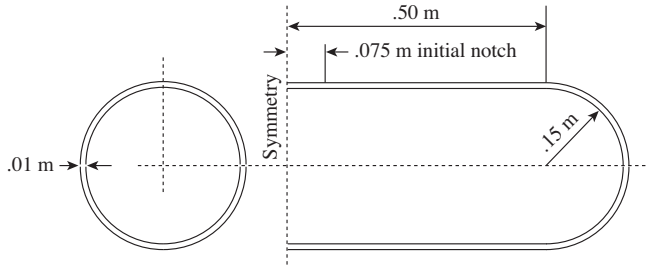


Fig. 20. Geometry and symmetry conditions for the pressure vessel simulation. The mesh is a three-dimensional thickened T-spline.

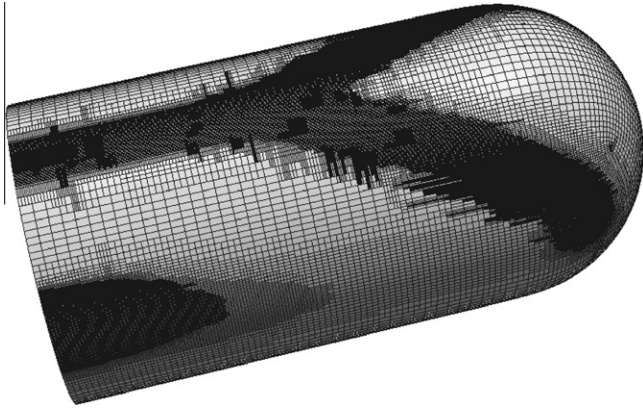


Fig. 21. The final mesh for the pressurized cylinder example problem. The volumetric mesh was constructed by thickening a mid-surface mesh. The refinement was performed using the adaptive refinement scheme describe in Section 4.4 which resulted in a final mesh containing 862,100 basis functions.

The model parameters are $\rho = 8000 \text{ kg/m}^3$, $E = 190 \text{ GPa}$, $\nu = 0.3$, $\mathcal{G}_c = 2.213 \times 10^4 \text{ J/m}^2$, and $k = 0$. The corresponding dilatational, shear, and Rayleigh wave speeds are $v_d = 5654 \text{ m/s}$, $v_s = 3022 \text{ m/s}$,

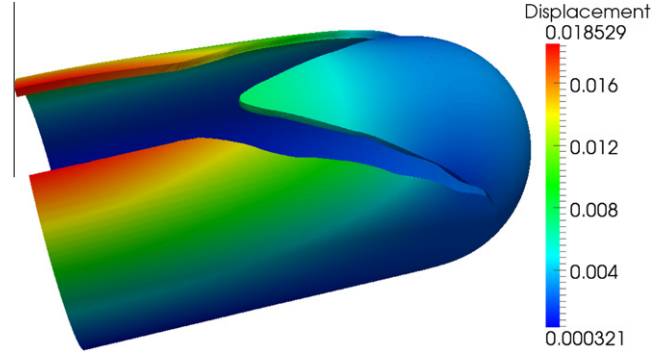


Fig. 23. A post-processed plot of the pressure vessel example at $t = 1.76 \times 10^{-3} \text{ s}$. The displacements have been scaled by a factor of 5 and areas of model where $c < 0.05$ have been removed from the plot. Displacement is measured in meters.

$v_R = 2803 \text{ m/s}$. The length scale was chosen to be $\ell_0 = 2.5 \times 10^{-3} \text{ m}$ leading to a maximum uniaxial stress of 298 MPa (see Section 2.3.1).

To construct the mesh, a C^2 -continuous cubic T-spline mid-surface was first modeled in Rhino, a commercial CAD software package, using the T-Splines, Inc., plugin. The initial mid-surface mesh had a mesh size of $h \approx 0.01 \text{ m}$. After export, the surface was thickened with C^1 -continuous quadratic functions such that there were eight Bézier elements (eleven functions) through the thickness. To get the final mesh, we used the adaptive refinement scheme describe in Section 4.4. The refinement was applied to the mid-surface mesh at each iteration until $h \approx \ell_0/2$ in the area of the crack. A new volume mesh was created from the updated mid-surface mesh at each iteration. The final mesh is shown in Fig. 21. This mesh contains 862,100 basis functions.

The simulations were performed using the staggered integration scheme described in Section 3.3.2 with the momentum equation being solved explicitly using the HHT- α method with $\alpha = -0.3$. An adaptive time step of $\Delta t = 0.9 \Delta t_{\text{crit}}$ was used (see Section 4.3 for a definition of Δt_{crit}). To compute Δt_{crit} , we used the power

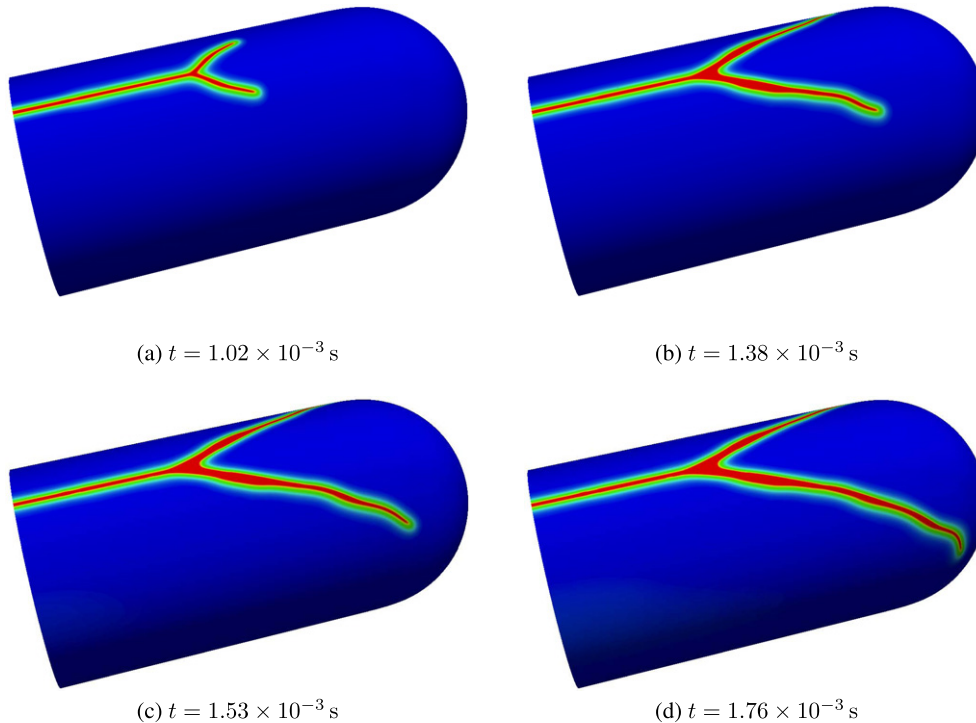


Fig. 22. The results of the pressurized cylinder example. The phase-field is shown.

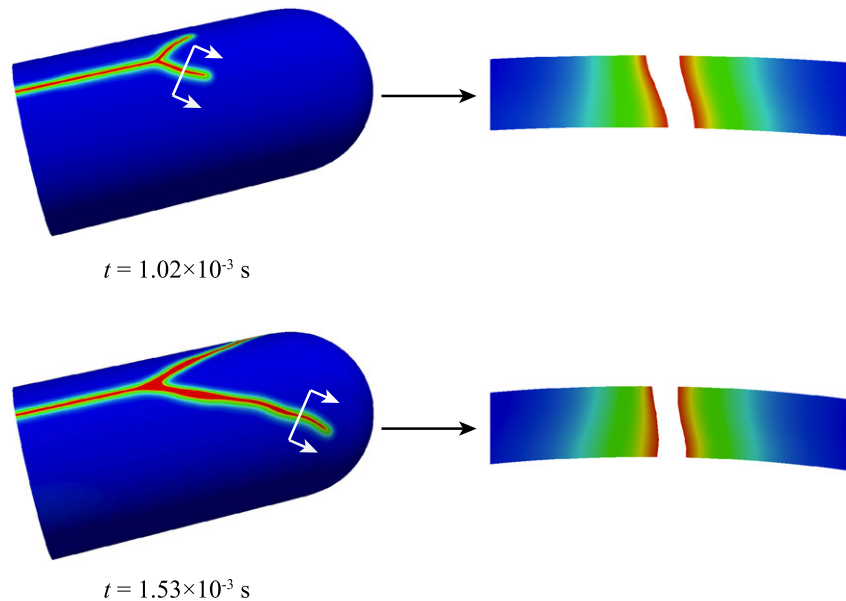


Fig. 24. Cross section views showing the three-dimensional phase-field profiles of the crack surfaces.

iteration algorithm presented by Benson [8]. The resulting phase-field is shown at several time intervals in Fig. 22. A post-processed plot of the model at $t = 1.76 \times 10^{-3}$ s is shown in Fig. 23 with the displacements scaled by a factor of 5 and the area of the model where $c < 0.05$ removed from the visualization.

Fig. 24 shows two cross-section views of the crack at different times in the simulation. These cross-sections show the ability of the phase-field model to capture three-dimensional characteristics of a crack. We emphasize that the computation for this three-dimensional model did not require any additional algorithmic complexity compared to the two-dimensional models shown previously.

Remark: This model demonstrates several key features of isogeometric analysis. First, the initial mid-surface model was constructed in a commercial CAD software package. This model was used directly to construct the analysis model, i.e., there is no intermediate meshing step. Second, the smoothness of the CAD geometry is represented exactly by the analysis model. Finally, refinement was performed directly on the CAD model and the exact CAD geometry was maintained at each iteration. This is illustrated in Fig. 21.

5. Conclusion

We have extended the phase-field model for quasi-static brittle fracture presented by Miehe et al. [37] to the dynamic case. The phase-field model provides a smooth representation of a crack and removes the requirement to numerically track discontinuities in the displacement field. The width of the phase-field approximation of a discrete crack is controlled by a length scale parameter. We have shown that this parameter also influences the critical stress at which crack nucleation occurs and should therefore be considered as a material parameter. To perform time integration of the dynamic model, we have presented both a monolithic and a staggered time integration scheme. The staggered scheme provides efficiency and flexibility in how the momentum equation is integrated and therefore holds greater potential for large three-dimensional problems. We note that, in general, dynamic crack propagation necessitates time steps of order the Courant number and therefore there is little to be gained from monolithic fully implicit approaches. In the staggered

scheme, the momentum equations can be treated explicitly and the phase-field equation can be efficiently solved with conjugate gradients in about 30 iterations, as we have experienced even for large problems. Consequently, a significant reduction of storage and computational effort ensues.

We have studied the behavior of the model by performing numerical experiments for crack propagation and branching. These examples have shown that the phase-field model can accurately capture complex dynamic crack propagation behavior in both two and three dimensions. In addition, we have proposed an adaptive local refinement strategy that allows for the efficient simulation of complex crack patterns. This refinement strategy takes advantage of the character of the phase-field evolution to determine when refinement is needed. We have demonstrated by numerical examples the effectiveness of this refinement scheme in the context of T-spline-based isogeometric analysis.

As a final example, we have shown that the combination of the phase-field model and local refinement strategy provides an effective method for simulating fracture in three-dimensional structures. The ability to simply and effectively model three-dimensional fracture is perhaps the most significant attribute of the phase-field model.

Acknowledgements

This work was supported by grants from the Office of Naval Research (N00014-08-1-0992), the Army Research Office (W911NF-10-1-0216), the National Science Foundation (CMI-0700807), and SINTEF (UTA10-000374). M.A. Scott was partially supported by an ICES CAM Graduate Fellowship. M.J. Borden was partially supported by Sandia National Laboratories. Sandia is a multiprogram laboratory operated by Sandia Corporation, a Lockheed Martin Company, for the United States Department of Energy's National Nuclear Security Administration under contract DE-AC04-94AL85000. This support is gratefully acknowledged.

The authors also acknowledge the Texas Advanced Computing Center (TACC) at The University of Texas at Austin for providing HPC and visualization resources that have contributed to the research results reported within this paper. URL: <http://www.tacc.utexas.edu>.

Appendix A. Modeling a preexisting crack in a continuous body

For the numerical examples discussed in this paper, a preexisting crack is used to initialize crack propagation. The initial crack is model as either a discrete crack in the geometry or as an induced crack in the phase-field. For the induced crack, an initial strain-history field is specified such that an initial crack in the phase-field is defined. To define the initial strain-history field we let l be a line that represents the discrete crack we wish to include and $d(\mathbf{x}, l)$ is the closest distance from \mathbf{x} to the line l . The strain-history field is then defined as

$$\mathcal{H}_0(\mathbf{x}) = B \begin{cases} \frac{\mathcal{G}_l}{4\ell_0} \left(1 - \frac{d(\mathbf{x}, l)}{\ell_0}\right) & d(\mathbf{x}, l) \leq \ell_0, \\ 0 & d(\mathbf{x}, l) > \ell_0, \end{cases} \quad (104)$$

where the magnitude of the scalar B can be determined by letting $d = 0$ and substituting \mathcal{H}_0 into (21)₂ with $k = 0$ and $\partial^2 c / \partial x_i = 0$ to get

$$B = \frac{1}{c} - 1. \quad (105)$$

In the examples presented above, we have chosen $c = 10^{-3}$ to be the value of the phase-field in the initial crack so that $B = 10^3$.

There are two important advantages to the current approach: First and foremost, initial cracks can be located anywhere in the domain without reference to the mesh. We believe this may prove highly advantageous in specifying complex surface cracks in three-dimensional bodies. A second advantage is that it can be easily utilized with non-interpolatory basis functions, such as are used in meshless methods and, in the examples presented here, isogeometric analysis.

Appendix B. Dimensionless form of the phase-field equations

To improve the conditioning and scaling of the fully coupled system of equations discussed in Section 3.3.1, we consider the strong form Eq. (21) in their dimensionless form. To arrive at the dimensionless formulation we define a length scale L_0 and time scale T_0 as

$$L_0 = \frac{\mathcal{G}_l}{C_h E}, \quad T_0 = L_0 \sqrt{\frac{\rho}{C_h E}}, \quad (106)$$

where the non-dimensional constant C_h is used to control the scaling of the problem. By introducing non-dimensional space and time coordinates, and a non-dimensional displacement field as

$$\mathbf{x}^* = \mathbf{x}/L_0, \quad t^* = t/T_0, \quad \mathbf{u}^* = \mathbf{u}/L_0, \quad (107)$$

we arrive at

$$\begin{cases} \frac{\partial \sigma_{ij}^*}{\partial x_j^*} = \frac{\partial^2 u_i^*}{\partial (t^*)^2}, \\ [4\ell_0^*(1 - k)\mathcal{H}^* + 1]c - 4(\ell_0^*)^2 \frac{\partial^2 c}{\partial (x_i^*)^2} = 1 \end{cases} \quad (108)$$

with

$$\sigma^* = \frac{\sigma}{C_h E}, \quad \mathcal{H}^* = \frac{\mathcal{H}}{C_h E}, \quad \ell_0^* = \frac{\ell_0}{L_0}. \quad (109)$$

In practice, we have found that choosing C_h such that the size of the elements in the mesh have an area equal to one yields good results.

Remark B.1. The same implementation can be used to compute with both the dimensional and non-dimensional forms of the equations. If the dimensional form of the equations has been implemented then the non-dimensional form can be computed by setting the material parameters $\mathcal{G}_c = 1$, $\rho = 1$, and $E = 1/C_h$; scaling

the input geometry by $1/L_0$; scaling the time steps by $1/T_0$; and using ℓ_0^* in place of ℓ_0 .

References

- [1] L. Ambrosio, V.M. Tortorelli, Approximation of functional depending on jumps by elliptic functional via Γ -convergence, *Commun. Pure Appl. Math.* 43 (8) (1990) 999–1036.
- [2] L. Ambrosio, V.M. Tortorelli, On the approximation of free discontinuity problems, *Boll. Un. Mat. Ital. B* (7) 6 (1) (1992) 105–123.
- [3] H. Amor, J.J. Marigo, C. Maurini, Regularized formulation of the variational brittle fracture with unilateral contact: numerical experiments, *J. Mech. Phys. Solids* 57 (8) (2009) 1209–1229.
- [4] I. Babuška, J.M. Melenk, The partition of unity method, *Int. J. Numer. Methods Engrg.* 40 (4) (1997) 727–758.
- [5] G. Bellettini, A. Coscia, Discrete approximation of a free discontinuity problem, *Numer. Funct. Anal. Optim.* 15 (3–4) (1994) 201–224.
- [6] T. Belytschko, H. Chen, J. Xu, G. Zi, Dynamic crack propagation based on loss of hyperbolicity and a new discontinuous enrichment, *Int. J. Numer. Methods Eng.* 58 (12) (2003) 1873–1905.
- [7] A. Benallal, J.-J. Marigo, Bifurcation and stability issues in gradient theories with softening, *Modell. Simul. Mater. Sci. Engrg.* 15 (1) (2007) S283.
- [8] D.J. Benson, Stable time step estimation for multi-material eulerian hydrocodes, *Comput. Methods Appl. Mech. Engrg.* 167 (1–2) (1998) 191–205.
- [9] D.J. Benson, Y. Bazilevs, M.C. Hsu, T.J.R. Hughes, A large deformation, rotation-free, isogeometric shell, *Comput. Methods Appl. Mech. Engrg.* 200 (13–16) (2011) 1367–1378.
- [10] M.J. Borden, M.A. Scott, J.A. Evans, T.J.R. Hughes, Isogeometric finite element data structures based on Bézier extraction of NURBS, *Int. J. Numer. Methods Engrg.* 87 (1–5) (2011) 15–47.
- [11] B. Bourdin, Image segmentation with a finite element method, *M2AN Math. Modell. Numer. Anal.* 33 (2) (1999) 229–244.
- [12] B. Bourdin, Numerical implementation of the variational formulation for quasi-static brittle fracture, *Interf. Free Bound.* 9 (3) (2007) 411–430.
- [13] B. Bourdin, G.A. Francfort, J.-J. Marigo, Numerical experiments in revisited brittle fracture, *J. Mech. Phys. Solids* 48 (4) (2000) 797–826.
- [14] B. Bourdin, G.A. Francfort, J.J. Marigo, The variational approach to fracture, *J. Elast.* 91 (1–3) (2008) 5–148.
- [15] B. Bourdin, C. Larsen, C. Richardson, A time-discrete model for dynamic fracture based on crack regularization, *Int. J. Fract.* 168 (2) (2011) 133–143.
- [16] A. Braides, Approximation of Free-Discontinuity Problems, Springer, Berlin, 1998.
- [17] S. Burke, C. Ortner, E. Süli, An adaptive finite element approximation of a variational model of brittle fracture, *SIAM J. Numer. Anal.* 48 (3) (2010) 980–1012.
- [18] J. Chung, G.M. Hulbert, A time integration algorithm for structural dynamics with improved numerical dissipation: the generalized-alpha method, *J. Appl. Mech.* 60 (2) (1993) 371–375.
- [19] G. Del Piero, G. Lancioni, R. March, A variational model for fracture mechanics: numerical experiments, *J. Mech. Phys. Solids* 55 (12) (2007) 2513–2537.
- [20] G.A. Francfort, N.Q. Le, S. Serfaty, Critical points of Ambrosio–Tortorelli Dirichlet case, *ESAIM: Control Optim. Calc. Var.* 15 (3) (2009) 576–598.
- [21] G.A. Francfort, J.J. Marigo, Revisiting brittle fracture as an energy minimization problem, *J. Mech. Phys. Solids* 46 (8) (1998) 1319–1342.
- [22] A. Giacomini, Ambrosio–Tortorelli approximation of quasi-static evolution of brittle fractures, *Calc. Var. Partial Diff. Equat.* 22 (2) (2005) 129–172.
- [23] H.M. Hilber, T.J.R. Hughes, R.L. Taylor, Improved numerical dissipation for time integration algorithms in structural dynamics, *Earthquake Engrg. Struct. Dyn.* 5 (1977) 283–292.
- [24] T.J.R. Hughes, *The Finite Element Method: Linear Static and Dynamic Finite Element Analysis*, Dover Publications, Mineola, NY, 2000.
- [25] T.J.R. Hughes, J.A. Cottrell, Y. Bazilevs, Isogeometric analysis: CAD, finite elements, NURBS, exact geometry and mesh refinement, *Comput. Methods Appl. Mech. Engrg.* 194 (2005) 4135–4195.
- [26] T.J.R. Hughes, A. Reali, G. Sangalli, Duality and unified analysis of discrete approximations in structural dynamics and wave propagation: comparison of p-method finite elements with k-method NURBS, *Comput. Methods Appl. Mech. Engrg.* 197 (49–50) (2008) 4104–4124.
- [27] T.J.R. Hughes, A. Reali, G. Sangalli, Efficient quadrature for NURBS-based isogeometric analysis, *Comput. Methods Appl. Mech. Engrg.* 199 (5–8) (2010) 301–313.
- [28] G.M. Hulbert, J. Chung, Explicit time integration algorithms for structural dynamics with optimal numerical dissipation, *Comput. Methods Appl. Mech. Engrg.* 137 (1996) 175–188.
- [29] J. Kalthoff, Modes of dynamic shear failure in solids, *Int. J. Fract.* 101 (1) (2000) 1–31.
- [30] J.F. Kalthoff, S. Winkler, Failure mode transition of high rates of shear loading, in: C.Y. Chiem, H.D. Kunze, L.W. Meyer, (Eds.), *Proceedings of the International Conference on Impact Loading and Dynamic Behavior of Materials*, vol. 1, 1987, pp. 185–195.
- [31] A. Karma, D.A. Kessler, H. Levine, Phase-field model of mode III dynamic fracture, *Phys. Rev. Lett.* 87 (4) (2001) 045501.

- [32] R. Krueger, Virtual crack closure technique: history, approach, and applications, *Appl. Mech. Rev.* 57 (2) (2004) 109–143.
- [33] G. Lancioni, G. Royer-Carfagni, The variational approach to fracture mechanics. a practical application to the French *Panthéon* in Paris, *J. Elast.* 95 (1) (2009) 1–30.
- [34] C.J. Larsen, Models for dynamic fracture based on griffith's criterion, in: K. Hackl (Ed.), *IUTAM Symposium on Variational Concepts with Applications to the Mechanics of Materials*, vol. 21, Springer, Netherlands, 2010, pp. 131–140.
- [35] C.J. Larsen, C. Ortner, E. Süli, Existence of solutions to a regularized model of dynamic fracture, *Math. Methods Models Appl. Sci.* 20 (7) (2010) 1021–1048.
- [36] X. Li, J. Zheng, T.W. Sederberg, T.J.R. Hughes, M.A. Scott, On linear independence of T-splines blending functions, *Comput. Aided Geometric Des.* 29 (1) (2012) 63–76.
- [37] C. Miehe, M. Hofacker, F. Welschinger, A phase field model for rate-independent crack propagation: robust algorithmic implementation based on operator splits, *Comput. Methods Appl. Mech. Engrg.* 199 (45–48) (2010) 2765–2778.
- [38] C. Miehe, F. Welschinger, M. Hofacker, Thermodynamically consistent phase-field models of fracture: variational principles and multi-field fe implementations, *Int. J. Numer. Methods Engrg.* 83 (10) (2010) 1273–1311.
- [39] I. Miranda, R.M. Ferencz, T.J.R. Hughes, An improved implicit-explicit time integration method for structural dynamics, *Earthquake Engrg. Struct. Dyn.* 18 (1989) 643–653.
- [40] N. Moës, J. Dolbow, T. Belytschko, A finite element method for crack growth without remeshing, *Int. J. Numer. Methods Engrg.* 46 (1) (1999) 131–150.
- [41] D. Mumford, J. Shah, Optimal approximations by piecewise smooth functions and associated variational problems, *Commun. Pure Appl. Math.* 42 (5) (1989) 577–685.
- [42] K. Pham, H. Amor, J.J. Marigo, C. Maurini, Gradient damage models and their use to approximate brittle fracture, *Int. J. Damage Mech.* 20 (4) (2011) 618–652.
- [43] K. Pham, J.J. Marigo, Construction and analysis of localized responses for gradient damage models in a 1d setting, *Vietnam J. Mech.* 31 (3–4) (2009) 233–246.
- [44] L. Piegl, W. Tiller, *The NURBS Book* (Monographs in Visual Communication), 2nd ed., Springer-Verlag, New York, 1997.
- [45] K. Ravi-Chandar, Dynamic fracture of nominally brittle materials, *Int. J. Fract.* 90 (1) (1998) 83–102.
- [46] K. Ravi-Chandar, W.G. Knauss, An experimental investigation into dynamic fracture: III. On steady-state crack propagation and crack branching, *Int. J. Fract.* 26 (2) (1984) 141–154.
- [47] K. Ravi-Chandar, J. Lu, B. Yang, Z. Zhu, Failure mode transitions in polymers under high strain rate loading, *Int. J. Fract.* 101 (2000) 33–72.
- [48] J.J.C. Remmers, R. de Borst, A. Needleman, The simulation of dynamic crack propagation using the cohesive segments method, *J. Mech. Phys. Solids* 56 (1) (2008) 70–92.
- [49] M.A. Scott, M.J. Borden, C.V. Verhoosel, T.J.R. Hughes, Isogeometric finite element data structures based on Bézier extraction of T-splines, *Int. J. Numer. Methods Engrg.* 88 (2) (2011) 126–156.
- [50] M.A. Scott, X. Li, T.W. Sederberg, T.J.R. Hughes, Local refinement of analysis-suitable T-splines, *Comput. Methods Appl. Mech. Engrg.* 213–216 (2012) 206–222.
- [51] S.-H. Song, H. Wang, T. Belytschko, A comparative study on finite element methods for dynamic fracture, *Comput. Mech.* 42 (2) (2008) 239–250.
- [52] C.V. Verhoosel, M.A. Scott, R. de Borst, T.J.R. Hughes, An isogeometric approach to cohesive zone modeling, *Int. J. Numer. Methods Engrg.* 88 (1–5) (2011) 336–360.
- [53] C.V. Verhoosel, M.A. Scott, T.J.R. Hughes, R. de Borst, An isogeometric analysis approach to gradient damage models, *Int. J. Numer. Methods Engrg.* 86 (1) (2011) 115–134.